Discrete element numerical simulation of mechanical properties of methane hydrate-bearing specimen considering deposit angles

*Bin Gong [1,2], Yujing Jiang [1, 2, *] Peng Yan [2], Sunhao Zhang [2]*

[1] Graduate School of Engineering, Nagasaki University, Nagasaki 852-8521, Japan;

[2] State Key Laboratory of Mining Disaster Prevention and Control Co-founded by Shandong Province and the Ministry of Science and Technology, Shandong University of Science and Technology, Qingdao 266590, China;

Corresponding author: Yujing Jiang

Corresponding Address: Bunkyo Machi 1-14, Nagasaki 852-8521, Japan.

Email: jiang@nagasaki-u.ac.jp

Phone: +81-080-3118-5202

Fax: +0532-86057957

Discrete element numerical simulation of mechanical properties of methane hydrate sediment considering deposit angles

Abstract:

Methane hydrate sediment (MHS) distributes under the seabed in different deposit angles according to the bottom simulating reflector (BSR) exhibitions. The mechanical properties of the combined sediment composed soil and MHS dominate the stability of the slope. In this work, the simulation model was generated considering the deposit angles, the confining pressures, the loading velocities and the hydrate saturation (S_h) by using discrete element method, and the mechanical response was studied. With deposit angle increasing, the peak strength increased first and then decreased. The elastic modulus decreased first and then increased with the increment of deposit angles. The peak strength and stiffness of sediments increased with increasing $S_{h.}$ The confining pressure enhanced the peak strength linearly, and the elastic modulus increased first and then decreased in a parabolic equation. Under different loading velocities conditions, the peak strength linearly increased and the elastic modulus logarithmically increased with increasing loading velocity.

Keywords: methane hydrate sediment, mechanical properties, deposit angle, compress test, discrete element method

1 Introduction

Methane hydrates are ice-like compound which methane gas melecules are trapped in a cage-like void of water melecules. The methane hydrate has many advantages compared with conventional fossil fuels such as high energy density, large reserves, and Green. Current research exhibited that more than half of the organic carbon mass in the world is stored in methan hydrates. The carbon mass storage trapped in methane hydrates is twice as much as all other fossil fuels combined. Methane hydrate is as a potential energy resource and the energy crisis can be solved if methane hydrate is exploited successfully. (Brugada et al., 2010; Kimoto et al., 2010; Kvenvolden and Lorenson, 2001; Sultan et al., 2004; Yu et al., 2012). Many countries like the United States, Japan, Canada, China, South Korea and India have performed extensive hydrate research (Collett et al., 2008; Dallimore and Collett, 1995; Dillon et al., 1994; Fujii et al., 2009; Koh et al., 2015; Wu et al., 2005). Methane hydrate is in existence under high-pressure and low-temperature conditions typically found in permafrost and deep seabed. The geological formations may be disrupted during the methane hydrate commercial production. For example, the dissociation of methane hydrate can trigger large-scale seafloor instabilities (Jin et al., 2016; Kleinberg et al., 2003; Nixon and Grozic, 2007; Pauli et al., 2003; Vedachalam et al., 2015; Xu and Germanovich, 2006). The greenhouse effect will be exacerbated if methane hydrate is disscociated and uncontrolled releases into the atmosphere (Brand et al., 2016; Paull et al., 2002; Zachos et al., 2008). Therefore, the mechanical properties of methane hydrate sediment (MHS) should be studied clearly before methane hydrate is exploited commercially and safely.

In order to commercially mine methane hydrate early, many tests of the mechanical properties of MHS have been conducted in the field and the laboratory by using various test methods. It is one of the best way to acquire the mechanical properties data of MHS using field samples or testing in-situ. In past decades, several in-situ tests of the mechanical properties of MHS were conducted. Winters et al. (2007) tested the acoustic properties and the shear properties of MHS drilled from the Mackenzie Delta. In their tests, the effect of the pore content, the sediment grain size and the pore pressure were considered. The shear strength was increased because of the existence of methane hydrate. The pore pressure decreased during shear tests in coarse-grained sediment, whereas the pore pressure increased in fine-graind sediment during shear test. Priest (2014) studied the impact of methane hydrate on the strength of host sediment drilled from the Krishna-Godavari Basin under the undrained conditions. The sediment containing methane hydate exhibited low shear strength. The shear strength increased with hydrate saturation (S_h) increasing. Yoneda (2015) carried out triaxial compression tests of sandy and clayey-silty MHS which were covered pressure coring in the Eastern Nankai Trough of Japan. In their tests, the excess pore pressure was always positive during compression tests for clayey-silty sediments under undrained conditions. The shear strength and stiffness of sandy sediments increased with S_h during drained compression tests. Jiang et al. (2017) investigated the mechanical properties of MHS in the Shenhu area of South China Sea using laboratoty geotechnical experiments. The results show that the moisture content and permeability decreased with shear strength increasing. The peak strength and elastic modulus of MHS increased with the increasing effective confining pressure.

Due to the limitations on the types of equipment and techniques in field tests, the mechanical properties of MHS were mainly studied using synthetic specimens in a laboratory. Previous experimental tests showed that the mechanical properties of sediment could change depending on the presence of hydrate by using a triaxial shear test, a direct shear test and a bending test (Ebinuma et al., 2005; Hyodo et al., 2008; Lee et al., 2010; Masui et al., 2005; Ohmura et al., 2002). Comparing the experimental results of field tests versus laboratory tests, it indicated that synthetic MHS had similar mechanical behaviors to those of the in-situ samples, to a certain extent. Masui et al. (2005) conducted a series of triaxial tests using the synthetic MHS generated with ice-sand and/or the water-sand mixture in their laboratory. In that study, the increment of S_h enhanced the shear strength, the secant elastic modulus, and cohesive force, and strain softening became more obvious with increasing S_h. Miyazaki (2010a, 2010b) examined the strain-rate dependence of the shear strength using artificial sediment in laboratory. In their research, it was found that the strain rate dependence of MHS is as strong as that of frozen sand. Hyodo (2013a, 2013b, 2014) reported the mechanical and dissociation response of cementation type MHS in undrained triaxial testing. Li et al. (2016) conducted a series of trial axial compressive tests of permafrost-associated methane hydrate-bearing sediments to study the mechanical properties under different exploiting methods. The results exhibited that both depressurization and heating will decrease the stability of methane hydrate-bearing sediments. Kajiyama et al. (2017) carried out a series of plane compression tests to study the effect of grain characteristics and fines contents on the mechanical properties of MHS. The test results indicated that the shear strength increased with fines content. The cohesion and friction angle of MHS increased with increasing S_h. Liu et al. (2017) proposed an easy and effective method to test the shear properties of MHS using a direct shear apparatus. The shear strength was strengthened due to the cementation effect of hydrates (Liu et al., 2019). Gong (2019) tested the mechanical properties of MHS in the laboratory using a multiple failure test method. The mechanical properties of MHS have been studied from different aspects in the above tests using various test apparatuses and methods. The test results indicated the mechanical properties of MHS depended on hydrate saturation significantly. However, the saturation of methane hydrate is difficult to maintain the same in every two experiments because of the limit of the experimental technology.

Due to the current monitoring technique limitation, the micromorphology of MHS during the test processes may not be capable of distinguishing. The Discrete Element Method (DEM, is a numerical method for computing the motion and effect of a large number of small particles) (Cundall and Strack,

1979) has been applicated widely in civil engineering, and this method can quantitatively describe the mechanical properties of MHS. The DEM supplied a new way to study the geotechnical problems of MHS. Many significant features of MHS, such as hydrate dissociation (Holtzman et al., 2009) or the hydrate distribution of pore-filling patterns (Brugada et al., 2010; Jung et al., 2012, 2010) or of cementation patterns (Jiang et al., 2014, 2013), can be investigated separately. It can be more intuitive to explain the destructive mechanism of the hydrate-sediment by using DEM. In recent years, several researchers have conducted studies on the mechanical properties of hydrate-sediment by using DEM. Brugada et al. (2010) investigated the micro-scale response of the mechanical behavior of pore-filling type MHS during triaxial compression test by using Particle Flow Code in 3 Dimensions (PFC3D). The simulation results exhibited that the existence of hydrate enhanced the frictional characteristic of MHS, rather than the cohesion characteristic. Jung et al. (2012) simulated two different kinds of methane hydrate distribution, which are patchy hydrate distribution and random pore-filling hydrate distribution, and investigated the mechanical properties of the two kinds of MHS. Sediments with patchy hydrate distribution exhibited lower shear strength than sediments with random pore-filling distributed hydrate.. Jiang et al. (2013) proposed a micro-bond model to study the mechanical response of bonding type methane hydrate and conducted biaxial tests using Particle Flow Code in 2 Dimensions (PFC2D). Jiang et al. (2015) studied the backpressure effect on the macroscopic mechanical properties of MHS using PFC2D. The simulation results showed that shear strength, small strain stiffness and shear dilation of MHS increased with the backpressure increasing. Yu et al. (2016) studied the effect of soil shape and the hydrate growth pattern on the mechanical properties during triaxial compression tests by using PFC3D. Wang et al. (2018) proposed a simulation method to generate pore-filling type hydrate by using PFC3D, and tested the mechanical properties under different confining pressure and S_h conditions. The peak strength and stiffness increased with increasing S_h and agreed with the experimental test results.

In nature, the methane hydrate-sediment generally deposits under loose soil or weakly bonded rock in a certain deposit angle. Methane hydrate in continental margins is commonly indicated by a prominent bottom-simulating reflector (BSR) that occurs a few hundred meters below the seabed. As shown in Fig. 1, the BSR can reflect the deposit condition of methane hydrate-sediment. In the figure, the methane hydrate-sediment deposits with a certain angle (Riedel et al., 2011). Due to the occurrence of environment change of methane hydrate, methane hydrate maybe decomposes. Methane maybe is emitted from the boundary above or/and below methane hydrate-sediment, as shown in Fig. 2 (Skarke et al., 2014). However, most of the previous mechanical properties research of MHS did not consider the effect of deposit angle of MHS. In this work, the mechanical response of the combined sediment composed soil and MHS is researched by using PFC2D considering hydrate saturation, deposit angle, confining pressure and loading velocity.

2 Simulation model generation and parameters determine

2.1 Simulation model generation

Due to the computational limitation, the initial size of the specimens was set to 5 mm in height and 2.5 mm in width. The soil specimen was initially prepared by generating 3498 balls with diameters ranging from 0.1 mm to 0.4 mm according to the particle size distribution curve of soil in a laboratory experiment (see Figure 3) (Masui et al., 2005) in a rectangle region with rigid frictionless walls. During this assembly generation stage, the initial value of porosity and inter-particle friction were set to 0.1 and 0.5, respectively. Once the DEM assembly has been generated, walls were moved to compress the specimen until the desired isotropic stress state (0.5 MPa) was achieved by the numerical servo-control mechanism.

Considering the generation process of MHS in the deep sea, it is assumed that hydrates were formed after the initial geostatic stress were carried by the soil skeleton. In this work, in order to simulate the generation of hydrates, the walls and soil particles were fixed first and then the radius of soil particles was shrunk to one-tenth of its original radius for generating hydrates particles more easily. Hydrate particles were randomly generated in the void space of MHS part of the rectangle area, followed soil particles were freed in all directions and expanded ten times to its original radius. Figure 4 shows an example of the specimen with the saturation of hydrate of 70% and the number of soil and hydrate grains was 12,000. In the figure, yellow circles and grey circles represent soil particles, and red circles represent hydrate particles. The volume of the upper half of soil particles equal to the volume of the lower half of soil particles. The angle between the boundary line, which is between the upper half of soil particles and the lower half of soil particles, and the horizontal line is defined as the deposit angle of methane hydrate. In the figure, the deposit angle of methane hydrate is expressed by ‘α’. Considering the cementation of hydrates, parallel bond contact model was set in hydrate-hydrate contacts and soil-hydrate contacts. Considering the rolling of particles, the rolling resistance model was set in soil-soil contacts. Completing the specimen generation, the generated specimen was compressed to the desired isotropic stress state (e.g. 1 MPa, 2 MPa, 3 MPa, 5 MPa, and 10 MPa).

2.2 Parameters selection and verification

According to the physical properties of drilled methane hydrate sediment from Nankai Trough (Santamarina et al., 2015), the density of soil particles was set at 2650 Kg/m^3 and the density of methane hydrate particles was set at 320 Kg/m^3. Based on the trial axial compressive test results conducted by Masui et, al. (2005), the parameters of particles and contacts were calibrated using the try out method. The relationship between stress versus strain in the simulations were compared with that in experiments under different S_h conditions, as shown in Fig. 5. The simulation results of stress-strain response present similar deformation characteristics in comparison with the experimental results obtained by Masui et al in the following aspects: （1）the strain softening become more and more evident with the increase of S_h; (2) both the elastic modulus and the maximum deviatoric stress increase gradually with S_h increasing, and the axial strain at the maximum deviatoric stress is around 2-4%, in good agreement with the experimental results; (3) the value of peak strength and elastic modulus in experimental test are almost coincident with those in simulation test, respectively. According to the above comparison, the simulation model can reflect the main characteristics of the mechanical properties of MHS, and the particle parameters used in simulation models are reasonable. The particle parameters used in simulations are listed in Table 1 and the contact parameters are listed in Table 2. The smooth lateral wall was given a normal stiffness of one-tenth of the mean particle stiffness in order to simulate soft confinement.

3 Test results and discussion

After the verification of the simulating model and the particle parameters, a series of bi-axial tests were conducted considering the hydrate saturation, the deposit angel, the confining pressure and the loading velocity. The simulation conditions of each group are shown in Table 3. All the test results of peak stress and elastic modulus are listed in the Appendix (Table 4).

3.1 Effect of the deposit angle

Methane hydrate generally generated in the void of soils and deposited under the deep seabed in a certain occurrence angle. The mechanical properties of MHS have been studied in previous research. In this section, the effect of the deposit angle on mechanical properties of MHS is introduced.

Fig. 6 shows the relationship between the deviatoric stress and axial the strain ratio during the shear test under the same loading velocity (1×10^{-6}m/s) and the same confining pressure (1 MPa) condition. In the figure, the strain softening tendency is similar in all cases under the same S_h condition. The peak stress shows fluctuations with increasing deposit angle. The fluctuation amplitude tends to become large with the increment of S_h. The initial elastic modulus and the secant elastic modulus (i.e., E_{50}) tend to be stable with S_h increasing. The peak stress and E_{50} are discussed in the following.

Fig. 7 shows the effect of the deposit angel on the peak stress and the elastic modulus considering loading velocities and hydrate saturations. The peak stress increased with increasing hydrate saturation. The peak stress increased slightly when the deposit angle is less than 45° under the condition that the loading velocity is less than 3×10^{-6}m/s， and then the peak stress decreased when the deposit angle was more than 45°. When the loading velocity was more than 5×10^{-6}m/s, the peak stress decreased after the deposit angle was more than 60°. The decreasing tendency of the peak stress turns more and more evident with increased hydrate saturation. The elastic modulus tended to decrease first and then increased before and after the deposit angle 45°.

Fig. 8 shows the effect of deposit angel on the peak stress and elastic modulus considering confining pressure and hydrate saturations. In all cases, the peak stress increased first and then decreased before and after the deposit angle 45°. When the confining pressure was 1 MPa, the elastic modulus exhibited fluctuation with increased deposit angle. Then elastic modulus increased with deposit angel increasing when the confining pressure was from 2 MPa to 5 MPa. When the confining pressure reached 10 MPa, the elastic modulus turns stable with deposit angle increasing.

Fig. 9 shows the displacement distribution of particles and the final deposit angle distribution of numerical samples after the shear test. The particles evenly moved in the horizontal direction when α=0° and the final deposit angle α'=0°. With deposit angle increasing, the movement of particles in soil part of the sample became more and more evident. The particles of soil part tended to move alongside the boundary line (the red dot line in the figure) more and more evident with the deposit angle increasing when the initial deposit angle was less than 45°~60°. When the initial deposit angle was more than 75°, the displacement distribution of soil particles was more evident than that of MHS particles. Because of the movement regular of soil particles, the elastic modulus tended to decrease first and then increased before and after the deposit angle 45°. The difference between α and α′ was defined $\Delta\alpha = \alpha - \alpha'$ here. The $\Delta\alpha$ were 0°, -4°, -7°, -8°, 1° and -4° respectively in the figure. Because the soil particles were easier to move alongside the boundary line when α>45°, the peak stress decreased after α>45° when the loading velocity was less than 3×10^{-6}m/s. Due to the loading velocity increasing, the soil particles moved alongside the boundary line easiest when α>60°. The peak stress decreased after α>60°.

Fig. 10 presents the contact force chains of numerical models with different deposit angels from 0° to 75° when shear test completing. The width of the force chains represents the value of contact forces, while the direction represents the direction of the contact force. With deposit angle increasing, the contact force chains increased generally before α<45°. The contact force chains decreased when the deposit angle was more than 60°. Due to the different distribution of the contact force chains with the deposit angle increasing, the peak stress and elastic modulus decreased after α>60°.

3.2 Effect of the methane hydrate saturation

The influence of hydrate saturation on methane hydrate-bearing sediments has been well studied. The larger the methane hydrate saturation, the larger the strength and the stiffness. The existence of hydrate will also affect the stress-strain curve of the specimen. In this section, the effect of methane hydrate saturation on the samples considering the deposit angle is discussed.

In Fig. 11, the peak stress and elastic modulus increased with the methane hydrate saturation increasing. The trend is consistent with the results of previous studies (Masui et al., 2008; Nagaeki et al., 2004; Sultan and Garziglia, 2011) because the methane hydrate concretes the soil particles and it needed bigger force to damage the cementation. With the methane hydrate saturation increasing, the magnitudes of peak stress and elastic moduli were 2.5 MPa ~ 5 MPa and 0.2 GPa~0.4 GPa when the loading velocity $v=1\times10^{-6}$m/s and confining pressure σ_3=1MPa. The magnitudes of peak stress and elastic moduli were 12 MPa ~ 15 MPa and 0.5 GPa~1.0 GPa when the loading velocity $v=10\times10^{-6}$m/s and confining pressure σ_3=1MPa.

Fig. 12 shows the effect of methane hydrate saturation on the peak stress and elastic modulus under different confining pressure conditions. With the methane hydrate saturation increasing, the magnitudes of peak stress and elastic moduli were 2.5 MPa ~ 5 MPa and 0.2 GPa~0.4 GPa when the loading velocity v=1×10^{-6}m/s and confining pressure σ_3=1MPa. The magnitudes of peak stress and elastic moduli were 9 MPa ~ 13 MPa and 0.3 GPa~0.8 GPa when the loading velocity v=1×10^{-6}m/s and confining pressure σ_3=10 MPa.

3.3 Effect of the confining pressure

The influence of confining pressure on methane hydrate-bearing sediments has been studied (Miyazaki et al., 2011). The strength and stiffness of the specimens were enhanced by effective confining pressure. The larger the effective confining pressure, the larger the strength and the stiffness. The confining pressure restrained specimen from deforming laterally. In this section, the effect of confining pressure on the samples considering the deposit angle is studied.

Fig. 13 presents the relationship between peak stress and elastic modulus versus confining pressure under the condition that methane hydrate saturation S_h=30% and loading velocity v=1×10^{-6}m/s~10×10^{-6}m/s. Fig. 14 presents the relationship between peak stress and elastic modulus versus confining pressure under the condition that the methane hydrate saturation S_h=30%~70% and loading velocity v=1×10^{-6}m/s. The peak stress increased with the confining pressure increasing. In Fig. 13, the magnitudes of peak stress were 3 MPa ~ 9 MPa when the loading velocity v=1×10^{-6}m/s and peak stress were 12 MPa ~ 25 MPa when the loading velocity v=10×10^{-6}m/s. In Fig. 14, the magnitudes of peak stress were 3 MPa ~ 9 MPa when t the methane hydrate saturation S_h=30% and peak stress were 12 MPa ~ 25 MPa when t the methane hydrate saturation S_h=70%. There was a linear relationship between the peak stress and confining pressure. The peak stress increased in accordance with the following linear equation:

$$\sigma_{\text{peak}} = b + a * c \tag{1}$$

where σ_{peak} is the peak stress, a and b is the coefficient, c represents the confining pressure. The coefficient b reflects the increasing rate of peak stress. In Fig. 13(a), when the loading velocity v=1×10^{-6}m/s and the methane hydrate saturation S_h=30%, the coefficient b=0.713. With the increment of loading velocity, the coefficient b increased gradually. When the loading velocity reached 10×10^{-6}m/s, the coefficient b=1.286 in Fig. 13(e). When the methane hydrate saturation S_h=70%, the coefficient b=0.813 in Fig. 14(e). It is attributed to the particles presenting a predominant vertical movement rather than horizontal movement. There was a parabolic relationship between elastic modulus and confining pressure as shown in Fig. 13(f)~(j) and Fig.

14(f)~(j). The elastic modulus increased first and then decreased with the confining pressure increasing.

According to the Mohr-Coulomb criterion, the shear strength can be expressed as follows:

$$\tau=\sigma\times\tan\varphi+c \tag{2}$$

where τ is the peak stress of the shear test, σ is the axial pressure of the shear test, φ is the internal friction angle and c is the cohesion.

The cohesion and internal friction angles of tested numerical specimens considering the methane hydrate saturation, deposit angle and loading velocity are listed in Appendix (Table 5). It is well accepted that the shear strength of the soil is jointly governed by the cohesion and internal friction angle. For MHS, the cohesion of MHS is the bonding force at the inter-particle level by cementing agents. The internal friction angle refers to the inter-particle friction for movement, rolling and rearrangement of sand grains bonded by hydrate. A rise in internal friction angle from 15.1° to 21.5°and cohesion from 0.8 MPa to 1.25 MPa when α=0°and S_h=30%~70% can be seen in Fig. 15(a) and (c). Internal friction angle increased from 15.1° to 23.25°and cohesion increased from 0.8 MPa to 4.14 MPa when α=0°and $v=1\times10^{-6}$m/s~10×10^{-6}m/s. The internal friction angle and cohesion increased with the increase of methane hydrate saturation and loading velocity. The relative relationship between the deposit angle versus the internal friction angle and the relationship between the cohesion and the deposit angle are not evident.

3.4 Effect of the loading velocity

For soil specimens, the high loading velocity will enhance the strength and the stiffness of the specimens. In this section, the effect of loading velocity on the strength and the stiffness of MHS was studied considering five loading velocity cases.

Fig. 16 presents the relationship between peak stress and elastic modulus versus loading velocity under the condition that methane hydrate saturation S_h=30% and confining pressure c=1 MPa~10 MPa. Fig. 17 presents the relationship between peak stress and elastic modulus versus confining pressure under the condition that the methane hydrate saturation S_h=30%~70% and loading velocity c=1 MPa. The peak stress increased with the loading velocity increasing. In Fig. 16, the magnitudes of peak stress were 2.5 MPa ~ 12.5 MPa when the loading velocity c=1 MPa and peak stress were 7.5 MPa ~ 25 MPa when the loading velocity c=10 MPa. In Fig. 17, the magnitudes of peak stress were 2.5 MPa ~ 12.5 MPa when t the methane hydrate saturation S_h=30% and peak stress were 2.5 MPa ~ 22.5 MPa when t the methane hydrate saturation S_h=70%. There was a linear relationship between the peak stress and confining pressure. The peak stress increased in accordance with the following linear equation:

$$\sigma_{\text{peak}} = b + a * v \tag{3}$$

where σ_{peak} is the peak stress, a and b is the coefficient, v represents the loading velocity. The coefficient b reflects the increasing rate of peak stress. In Fig. 16(a), when the confining pressure c=1 MPa and the methane hydrate saturation S_h=30%, the coefficient b=1.11. With the increment of loading velocity, the coefficient b increased gradually. When the loading velocity reached 10 MPa, the coefficient b=1.71 in Fig. 16(e). When the methane hydrate saturation S_h=70%, the coefficient b=1.77 in Fig. 17(e). It is attributed to the particles presenting a predominant vertical movement rather than a horizontal movement with the loading velocity increasing in the vertical direction. There was an exponential relationship between elastic modulus and confining pressure as shown in Fig. 16(f)~(j) and Fig. 17(f)~(j). The elastic modulus increased first and then decreased with the confining pressure increasing.

4 Conclusions and prospects

Methane hydrate distributes under the seabed in different deposit angle according to the BSR exhibitions. The non-bonded soil deposits above and/or below the MHS, and the mechanical properties of the combined sediment composed soil and MHS dominate the stability of the slope under the deep sea. In this work, the combined sediment model was generated considering the deposit angles (0°, 15°, 30°, 45°, 60°and 75°), the confining pressures (1MPa, 2MPa,3MPa, 5MPa and 10MPa), the loading velocities (1×10^{-6}m/s, 2×10^{-6}m/s, 3×10^{-6}m/s, 5×10^{-6}m/s and 10×10^{-6}m/s) and the hydrate saturation (30%, 40%, 50%, 60% and 70%) by using discrete element method.

The peak stress increased slightly when the deposit angle is less than 45° under the condition that the loading velocity is less than 3×10^{-6}m/s， and then the peak stress decreased when the deposit angle was more than 45°. When the loading velocity was more than 5×10^{-6}m/s, the peak stress decreased after the deposit angle was more than 60°. The decreasing tendency of the peak stress turns more and more evident with increased hydrate saturation. The elastic modulus tended to decrease first and then increased before and after the deposit angle 45°. The elastic modulus decreases first and then increases with the increment of the deposit angle. The peak strength and stiffness of the combined sediment increased with increasing $S_{h.}$

There was a linear relationship between the peak stress and confining pressure. There was a parabolic relationship between elastic modulus and confining pressure and the elastic modulus increased first and then decreased with the confining pressure increasing before and after 6 MPa. The internal friction angle and cohesion increased with the increase of methane hydrate saturation and loading velocity. The relative relationship between the deposit angle versus the internal friction angle and the relationship between the cohesion and the deposit angle are not evident. There was a linear relationship between the peak stress and loading velocity. There was an exponential relationship between elastic modulus and loading velocity.

The mechanical response of MHS is discussed without considering water pressure and hydrate dissociation in this work. The undrained shear behavior of MHS is important to assess the slope stability in which the permeability is low for water and gas. In future studies, the deformation mechanism of MHS under undrained condition will be tested. And more detailed deformation responses at the particle scale before and after dissociation of hydrate will be discussed.

Acknowledgments

This study has been partially funded by the National Natural Science Foundation of China (Grant No.51804180), China Scholarship Council (CSC NO. 201608370083), the Key Research and Development Plan of Shandong Province (Grant NO. 2018GSF116007). These supports are gratefully acknowledged.

References

Brand, U., Blamey, N., Garbelli, C., Griesshaber, E., Posenato, R., Angiolini, L., Azmy, K., Farabegoli, E., Came, R., 2016. Methane Hydrate: Killer cause of Earth's greatest mass extinction. Palaeoworld 25, 496–507.

Brugada, J., Cheng, Y.P., Soga, K., Santamarina, J.C., 2010. Discrete element modelling of geomechanical behaviour of methane hydrate soils with pore-filling hydrate distribution. Granul. Matter 12, 517–525.

Collett, T., Riedel, M., Cochran, J.R., Boswell, R., Kumar, P., Sathe, A. V, 2008. Indian continental margin gas hydrate prospects: results of the Indian National Gas Hydrate Program (NGHP) expedition 01.

Cundall, P.A., Strack, O.D.L., 1979. A discrete numerical model for granular assemblies. geotechnique 29, 47–65.

Dallimore, S.R., Collett, T.S., 1995. Intrapermafrost gas hydrates from a deep core hole in the Mackenzie Delta, Northwest Territories, Canada. Geology 23, 527–530.

Dillon, W.P., Lee, M.W., Coleman, D.F., 1994. Identification of marine hydrates in situ and their distribution off the Atlantic coast of the United States. Ann. N. Y. Acad. Sci. 715, 364–380.

Ebinuma, T., Kamata, Y., Minagawa, H., Ohmura, R., Nagao, J., Narita, H., 2005. Mechanical properties of sandy sediment containing methane hydrate, in: Proceedings of Fifth International Conference on Gas Hydrates, Pap. pp. 958–961.

Fujii, T., Nakamizu, M., Tsuji, Y., Namikawa, T., Okui, T., Kawasaki, M., Ochiai, K., Nishimura, M., Takano, O., 2009. Methane-hydrate occurrence and saturation confirmed from core samples, eastern Nankai Trough, Japan.

Gong, B., Jiang, Y., Chen, L., 2019. Feasibility investigation of the mechanical behavior of methane hydrate-bearing specimens using the multiple failure method. J. Nat. Gas Sci. Eng. 102915.

Holtzman, R., Silin, D.B., Patzek, T.W., 2009. Mechanical properties of granular materials: A variational approach to grain-scale simulations. Int. J. Numer. Anal. methods Geomech. 33, 391–404.

Hyodo, M., Li, Y., Yoneda, J., Nakata, Y., Yoshimoto, N., Kajiyama, S., Nishimura, A., Song, Y., 2014. A comparative analysis of the mechanical behavior of carbon dioxide and methane hydrate-bearing sediments. Am. Mineral. 99, 178–183.

Hyodo, M., Li, Y., Yoneda, J., Nakata, Y., Yoshimoto, N., Nishimura, A., Song, Y., 2013a. Mechanical behavior of gas-saturated methane hydrate-bearing sediments. J. Geophys. Res. solid earth 118, 5185–5194.

Hyodo, M., Nakata, Y., Yoshimoto, N., Yoneda, J., 2008. Shear strength of methane hydrate bearing sand and its deformation during dissociation of methane hydrate, in: Proc. of 4th Int. Symp. on Deformation Characteristics of Geomaterials. pp. 549–556.

Hyodo, M., Yoneda, J., Yoshimoto, N., Nakata, Y., 2013b. Mechanical and dissociation properties of methane hydrate-bearing sand in deep seabed. Soils Found. 53, 299–314. https://doi.org/10.1016/j.sandf.2013.02.010

Jiang, J., Shen, Z., Jia, Y., 2017. Physical and Mechanical Properties of Surface Sediments and methane hydrate-bearing sediments in the Shenhu area of South China Sea, in: AGU Fall Meeting Abstracts.

Jiang, M., Zhu, F., Liu, F., Utili, S., 2014. A bond contact model for methane hydrate-bearing sediments with interparticle cementation. Int. J. Numer. Anal. Methods Geomech. 38, 1823–1854.

Jiang, M., Zhu, F., Utili, S., 2015. Investigation into the effect of backpressure on the mechanical behavior of methane-hydrate-bearing sediments via DEM analyses. Comput. Geotech. 69, 551–563.

Jiang, M.J., Liu, F., Zhu, F., Xiao, Y., 2013. A simplified contact model for sandy grains cemented with methane hydrate, in: Proceedings of the 18th International Conference on Soil Mechanics and Geotechnical Engineering. pp. 1015–1018.

Jin, G., Xu, T., Xin, X., Wei, M., Liu, C., 2016. Numerical evaluation of the methane production from unconfined gas hydrate-bearing sediment by thermal stimulation and depressurization in Shenhu area, South China Sea. J. Nat. Gas Sci. Eng. 33, 497–508.

Jung, J., Santamarina, J.C., Soga, K., 2012. Stress-strain response of hydrate-bearing sands: Numerical study using discrete element method simulations. J. Geophys. Res. solid earth 117.

Jung, J.W., Espinoza, D.N., Santamarina, J.C., 2010. Properties and phenomena relevant to CH4-CO2 replacement in hydrate-bearing sediments. J. Geophys. Res. Solid Earth 115.

Kajiyama, S., Hyodo, M., Nakata, Y., Yoshimoto, N., Wu, Y., Kato, A., 2017. Shear behaviour of methane hydrate bearing sand with various particle characteristics and fines. Soils Found. 57, 176–193.

Kimoto, S., Oka, F., Fushita, T., 2010. A chemo-thermo-mechanically coupled analysis of ground deformation induced by gas hydrate dissociation. Int. J. Mech. Sci. 52, 365–376. https://doi.org/10.1016/j.ijmecsci.2009.10.008

Kleinberg, R.L., Flaum, C., Griffin, D.D., Brewer, P.G., Malby, G.E., Peltzer, E.T., Yesinowski, J.P., 2003. Deep sea NMR: Methane hydrate growth habit in porous media and its relationship to hydraulic permeability, deposit accumulation, and submarine slope stability. J. Geophys. Res. Solid Earth 108.

Koh, D., Ahn, Y., Kang, H., Park, S., Lee, J.Y., Kim, S., Lee, J., Lee, H., 2015. One-dimensional productivity assessment for on-field methane hydrate production using CO2/N2 mixture gas. AIChE J. 61, 1004–1014.

Kvenvolden, K.A., Lorenson, T.D., 2001. The global occurrence of natural gas hydrate. Nat. Gas Hydrates Occur. Distrib. Detect. Occur. Distrib. Detect. 124, 3–18.

Lee, J.Y., Francisca, F.M., Santamarina, J.C., Ruppel, C., 2010. Parametric study of the physical properties of hydrate-bearing sand, silt, and clay sediments: 2. Small-strain mechanical properties. J. Geophys. Res. Solid Earth 115.

Li, Y., Liu, W., Zhu, Y., Chen, Y., Song, Y., Li, Q., 2016. Mechanical behaviors of permafrost-associated methane hydrate-bearing sediments under different mining methods. Appl. Energy 162, 1627–1632.

Liu, L., Dai, S., Ning, F., Cai, J., Liu, C., Wu, N., 2019. Fractal characteristics of unsaturated sands− implications to relative permeability in hydrate-bearing sediments. J. Nat. Gas Sci. Eng.

Liu, Z., Wei, H., Peng, L., Wei, C., Ning, F., 2017. An easy and efficient way to evaluate mechanical properties of gas hydrate-bearing sediments: The direct shear test. J. Pet. Sci. Eng. 149, 56–64.

Masui, A., Haneda, H., Ogata, Y., Aoki, K., 2005. The effect of saturation degree of methane hydrate on the shear strength of synthetic methane hydrate sediments, in: Proceedings of the 5th International Conference on Gas Hydrates, Trondheim, Norway. pp. 657–663.

Masui, A., Miyazaki, K., Haneda, H., Ogata, Y., Aoki, K., 2008. Mechanical properties of natural gas hydrate bearing sediments retrieved from eastern Nankai trough, in: Offshore Technology Conference. Offshore Technology Conference.

Miyazaki, K., Masui, A., Aoki, K., Sakamoto, Y., Yamaguchi, T., Okubo, S., 2010a. Strain-rate dependence of triaxial compressive strength of artificial methane-hydrate-bearing sediment. Int. J. Offshore Polar Eng. 20.

Miyazaki, K., Masui, A., Sakamoto, Y., Tenma, N., Yamaguchi, T., 2010b. Effect of confining pressure on triaxial compressive properties of artificial methane hydrate bearing sediments, in: Offshore Technology Conference. Offshore Technology Conference.

Miyazaki, K., Tenma, N., Aoki, K., Sakamoto, Y., Yamaguchi, T., 2011. Effects of confining pressure on mechanical properties of artificial methane-hydrate-bearing sediment in triaxial compression test. Int. J. Offshore Polar Eng. 21.

Nagaeki, J., Jiang, Y., Tanabashi, Y., 2004. Compression strength and deformation behavior of methane hydrate specimen, in: The First Sino-Japan Seminar for the Graduate Student in Civil Engineering, Shanghai, China. pp. 16–20.

Nishimura, A., Hyodo, M., Nakata, Y., Li, Y., Yoshimoto, N., Yoneda, J., 2013. Effects of dissociation on the shear strength and deformation behavior of methane hydrate-bearing sediments. Mar. Pet. Geol. 51, 52–62. https://doi.org/10.1016/j.marpetgeo.2013.11.015

Nixon, M.F., Grozic, J.L.H., 2007. Submarine slope failure due to gas hydrate dissociation: a preliminary quantification. Can. Geotech. J. 44, 314–325.

Ohmura, R., Shigetomi, T., Mori, Y.H., 2002. Bending tests on clathrate hydrate single crystals. Philos. Mag. A 82, 1725–1740.

Pauli, C.K., Ussler, W.I.I.I., Dillon, W.P., 2003. Potential role of gas hydrate decomposition in generating submarine slope failures: Chapter 12.

Paull, C.K., Brewer, P.G., Ussler, W., Peltzer, E.T., Rehder, G., Clague, D., 2002. An experiment demonstrating that marine slumping is a mechanism to transfer methane from seafloor gas-hydrate deposits into the upper ocean and atmosphere. Geo-Marine Lett. 22, 198–203.

Priest, J.A., Clayton, C.R.I., Rees, E.V.L., 2014. Potential impact of gas hydrate and its dissociation on the strength of host sediment in the Krishna–Godavari Basin. Mar. Pet. Geol. 58, 187–198.

Riedel, M., Collett, T.S., Shankar, U., 2011. Documenting channel features associated with gas hydrates in the Krishna–Godavari Basin, offshore India. Mar. Geol. 279, 1–11.

Santamarina, J.C., Dai, S., Terzariol, M., Jang, J., Waite, W.F., Winters, W.J., Nagao, J., Yoneda, J., Konno, Y., Fujii, T., 2015. Hydro-bio-geomechanical properties of hydrate-bearing sediments from Nankai Trough. Mar. Pet. Geol. 66, 434–450.

Skarke, A., Ruppel, C., Kodis, M., Brothers, D., Lobecker, E., 2014. Widespread methane leakage from the sea floor on the northern US Atlantic margin. Nat. Geosci. 7, 657.

Sultan, N., Cochonat, P., Foucher, J.-P., Mienert, J., 2004. Effect of gas hydrates melting on seafloor slope instability. Mar. Geol. 213, 379–401.

Sultan, N., Garziglia, S., 2011. Geomechanical constitutive modelling of gas-hydrate-bearing sediments, in: Proceedings of the 7th International Conference on Gas Hydrates (ICGH 2011), Edinburgh, Scotland, United Kingdom, July. pp. 17–21.

Vedachalam, N., Ramesh, S., Jyothi, V.B.N., Prasad, N.T., Ramesh, R., Sathianarayanan, D., Ramadass, G.A., Atmanand, M.A., 2015. Evaluation of the depressurization based technique for methane hydrates reservoir dissociation in a marine setting, in the Krishna Godavari Basin, east coast of India. J. Nat. Gas Sci. Eng. 25, 226–235.

Wang, H., Zhou, B., Xue, S., Lin, Y., 2018. Discrete Element Simulation Analysis of Mechanical Behavior of the Gas Hydrate-Bearing Sediments.

Winters, W.J., Waite, W.F., Mason, D.H., Gilbert, L.Y., Pecher, I.A., 2007. Methane gas hydrate effect on sediment acoustic and strength properties. J. Pet. Sci. Eng. 56, 127–135.

Wu, S., Zhang, G., Huang, Y., Liang, J., Wong, H.K., 2005. Gas hydrate occurrence on the continental slope of the northern South China Sea. Mar. Pet. Geol. 22, 403–412.

Xu, W., Germanovich, L.N., 2006. Excess pore pressure resulting from methane hydrate dissociation in marine sediments: A theoretical approach. J. Geophys. Res. Solid Earth 111.

Yoneda, J., Masui, A., Konno, Y., Jin, Y., Egawa, K., Kida, M., Ito, T., Nagao, J., Tenma, N., 2015. Mechanical behavior of hydrate-bearing pressure-core sediments visualized under triaxial compression. Mar. Pet. Geol. 66, 451–459.

Yu, Y., Cheng, Y.P., Xu, X., Soga, K., 2016. Discrete element modelling of methane hydrate soil sediments using elongated soil particles. Comput. Geotech. 80, 397–409.

Yu, Y., Yang, J., Chen, B., 2012. The smart grids in China—A review. Energies 5, 1321–1338.

Zachos, J.C., Dickens, G.R., Zeebe, R.E., 2008. An early Cenozoic perspective on greenhouse warming and carbon-cycle dynamics. Nature 451, 279.

Table 1. Mechanical parameters of particles in simulation

Property	**Soil**	**Methane hydrate**
Density(Kg/m^3)	2650	320
Particle sizes, D(mm)	0.01-0.4	0.006
Normal stiffness k_n (N/m)	1e8	1e5
Shear stiffness k_s (N/m)	1e8	1e5
Inter-particle friction μ	0.7	0.75

Table 2. Mechanical parameters of contacts in simulation

Property	**Soil-Hydrate**	**Soil-Soil**	**Hydrate-Hydrate**
Friction μ	0.15	0.5	0.15
Normal stiffness k_n (N/m)	1e5	3e8	1e5
Shear stiffness k_s (N/m)	1e4	3e7	1e4
Tension strength (N)	3e6		3e6
Cohesion (N)	5e6		5e6
Friction angle	10		10
Rolling resistance coefficient （μ_r）		0.6	

Table 3. Simulation conditions of each group

parameters						
Deposit angle (°)	0	15	30	45	60	75
Hydrate Saturation (%)	30	40	50	60	70	
Confining pressure (MPa)	1	2	3	5	10	
Loading velocity (m/s)	1×10^{-6}	2×10^{-6}	3×10^{-6}	5×10^{-6}	10×10^{-6}	

Appendix:

Table 4 The peak strength and elastic modulus of specimens under different simulation conditions

No.	α (°)	σ (MPa)	v (1e-6m/s)	S_h=30%		S_h=40%		S_h=50%		S_h=60%		S_h=70%	
				P (MPa)	E_{50} (GPa)	P (MPa)	E_{50} (GPa)	P (MPa)	E_{50} (GPa)	P (MPa)	E_{50} (GPa)	P (MPa)	E_{50} (GPa)
1	0	1	1	2.57	0.20	3.16	0.25	3.67	0.30	4.26	0.32	4.80	0.34
2	0	1	2	3.97	0.26	5.03	0.32	5.89	0.38	6.65	0.41	7.60	0.43
3	0	1	3	5.26	0.30	6.51	0.38	7.58	0.44	8.82	0.48	9.68	0.51
4	0	1	5	7.60	0.37	9.15	0.46	10.66	0.52	12.19	0.57	14.03	0.62
5	0	1	10	12.94	0.49	14.97	0.64	17.53	0.71	19.19	0.82	22.56	0.93
6	0	2	1	3.61	0.25	4.32	0.30	4.94	0.36	5.54	0.41	6.16	0.45
7	0	2	2	5.20	0.32	6.33	0.39	7.46	0.44	8.56	0.51	9.50	0.54
8	0	2	3	6.64	0.36	8.14	0.45	9.54	0.52	10.94	0.59	12.26	0.63
9	0	2	5	9.29	0.43	11.33	0.43	13.34	0.59	15.01	0.68	16.74	0.74
10	0	2	10	15.02	0.55	18.24	0.55	20.64	0.84	22.87	0.92	25.52	1.04
11	0	3	1	4.60	0.29	5.39	0.34	5.91	0.42	6.81	0.46	7.38	0.53
12	0	3	2	6.39	0.35	7.65	0.43	8.73	0.51	10.05	0.57	11.06	0.65
13	0	3	3	8.05	0.42	9.61	0.51	11.22	0.58	12.88	0.64	14.16	0.73
14	0	3	5	10.98	0.48	13.07	0.60	14.92	0.68	17.03	0.77	19.13	0.84
15	0	3	10	17.11	0.63	20.41	0.81	23.31	0.93	25.46	1.08	28.56	1.11
16	0	5	1	6.14	0.34	7.09	0.39	7.84	0.49	8.66	0.54	9.26	0.63
17	0	5	2	8.23	0.42	9.65	0.50	11.18	0.61	12.43	0.67	13.56	0.75
18	0	5	3	10.04	0.48	12.10	0.57	13.86	0.68	15.69	0.75	17.39	0.81
19	0	5	5	13.26	0.56	15.82	0.67	18.50	0.77	20.82	0.88	23.25	0.94
20	0	5	10	20.43	0.69	24.26	0.87	27.23	1.05	31.26	1.14	33.68	1.30
21	0	10	1	8.91	0.30	10.07	0.33	10.76	0.40	11.89	0.42	12.65	0.48
22	0	10	2	11.23	0.37	12.96	0.43	14.35	0.52	16.21	0.54	17.51	0.64
23	0	10	3	13.19	0.44	15.62	0.50	17.78	0.61	20.20	0.63	21.79	0.74
24	0	10	5	16.86	0.54	20.06	0.62	23.13	0.72	26.02	0.78	28.73	0.87
25	0	10	10	24.79	0.67	30.06	0.83	33.98	0.94	37.93	1.04	41.67	1.21
26	15	1	1	2.71	0.22	3.19	0.24	3.63	0.29	4.32	0.33	4.93	0.33
27	15	1	2	4.22	0.28	5.18	0.30	5.71	0.39	6.93	0.41	7.65	0.44
28	15	1	3	5.55	0.32	6.77	0.35	7.56	0.45	8.81	0.48	10.03	0.51
29	15	1	5	8.02	0.39	9.39	0.45	10.72	0.54	11.93	0.61	13.67	0.61
30	15	1	10	13.10	0.55	15.36	0.62	18.26	0.74	19.81	0.83	21.23	0.88
31	15	2	1	3.76	0.26	4.26	0.29	4.85	0.37	5.57	0.40	6.29	0.44
32	15	2	2	5.43	0.33	6.31	0.39	7.33	0.46	8.57	0.50	9.55	0.54
33	15	2	3	7.03	0.37	8.08	0.44	9.48	0.53	10.82	0.59	12.33	0.61
34	15	2	5	9.79	0.46	11.37	0.46	13.34	0.64	14.58	0.67	16.41	0.75
35	15	2	10	15.64	0.60	17.94	0.60	21.12	0.88	22.53	0.92	24.99	0.99
36	15	3	1	4.67	0.30	5.24	0.34	5.92	0.42	6.75	0.45	7.47	0.52
37	15	3	2	6.53	0.37	7.46	0.43	8.76	0.52	9.94	0.57	11.29	0.61
38	15	3	3	8.22	0.43	9.55	0.49	11.20	0.58	12.44	0.64	14.28	0.70
39	15	3	5	11.11	0.51	13.04	0.59	15.34	0.69	16.66	0.75	18.71	0.82

40	15	3	10	17.15	0.65	20.28	0.80	23.27	0.91	25.96	0.97	27.98	1.12
41	15	5	1	6.42	0.35	7.04	0.40	7.62	0.49	8.57	0.55	9.60	0.58
42	15	5	2	8.60	0.43	9.81	0.49	10.92	0.60	12.35	0.66	13.80	0.73
43	15	5	3	10.60	0.48	12.15	0.57	13.85	0.69	15.36	0.75	17.15	0.82
44	15	5	5	13.93	0.58	16.19	0.67	18.97	0.78	20.05	0.88	20.05	0.88
45	15	5	10	20.77	0.76	24.11	0.87	28.12	1.07	31.11	1.08	33.05	1.20
46	15	10	1	9.66	0.29	10.07	0.33	10.96	0.38	11.71	0.44	12.76	0.46
47	15	10	2	11.96	0.37	13.13	0.43	14.49	0.51	15.90	0.57	17.75	0.60
48	15	10	3	13.97	0.44	15.69	0.51	17.68	0.60	19.58	0.66	21.73	0.69
49	15	10	5	17.53	0.54	20.51	0.60	23.10	0.72	25.98	0.78	28.36	0.83
50	15	10	10	25.85	0.73	29.92	0.82	33.96	1.00	37.98	1.11	41.06	1.12
51	30	1	1	2.69	0.21	3.14	0.26	3.71	0.28	4.34	0.35	4.78	0.32
52	30	1	2	4.22	0.28	5.00	0.33	5.96	0.37	6.81	0.43	7.58	0.42
53	30	1	3	5.48	0.34	6.70	0.39	7.96	0.43	8.65	0.51	9.92	0.48
54	30	1	5	7.88	0.41	9.55	0.47	11.29	0.51	11.98	0.60	13.68	0.58
55	30	1	10	13.10	0.57	15.60	0.66	18.23	0.72	20.17	0.80	21.47	0.84
56	30	2	1	3.76	0.25	4.18	0.32	4.91	0.38	5.58	0.43	6.02	0.44
57	30	2	2	5.41	0.32	6.39	0.40	7.61	0.47	8.61	0.53	9.60	0.52
58	30	2	3	6.91	0.36	8.36	0.45	9.78	0.54	11.09	0.60	12.66	0.58
59	30	2	5	9.59	0.46	11.94	0.46	13.63	0.62	14.55	0.73	17.14	0.68
60	30	2	10	15.64	0.59	18.57	0.59	21.51	0.85	23.47	0.94	25.40	0.97
61	30	3	1	4.59	0.31	5.16	0.37	6.03	0.44	6.79	0.49	7.23	0.54
62	30	3	2	6.40	0.37	7.60	0.45	8.95	0.54	10.02	0.59	11.40	0.61
63	30	3	3	7.94	0.43	9.65	0.52	11.23	0.61	12.70	0.67	14.65	0.67
64	30	3	5	11.12	0.50	13.09	0.62	15.23	0.72	16.63	0.81	19.57	0.79
65	30	3	10	17.50	0.63	20.78	0.78	23.85	0.94	26.39	1.03	28.02	1.08
66	30	5	1	6.27	0.35	6.85	0.44	7.82	0.53	8.61	0.56	9.35	0.63
67	30	5	2	8.35	0.44	9.52	0.53	11.27	0.63	12.39	0.68	13.67	0.75
68	30	5	3	10.10	0.50	11.70	0.60	13.98	0.71	15.51	0.77	17.30	0.82
69	30	5	5	13.51	0.58	15.79	0.69	18.58	0.83	20.38	0.93	23.14	0.94
70	30	5	10	20.82	0.71	24.38	0.86	28.54	1.05	31.42	1.14	33.15	1.22
71	30	10	1	9.15	0.29	10.04	0.34	10.86	0.40	11.86	0.45	12.63	0.50
72	30	10	2	11.35	0.38	12.99	0.45	14.48	0.54	15.97	0.61	17.56	0.65
73	30	10	3	13.47	0.44	15.75	0.54	18.12	0.63	19.62	0.70	21.86	0.74
74	30	10	5	17.43	0.53	20.42	0.66	23.60	0.76	26.17	0.84	28.75	0.88
75	30	10	10	25.66	0.69	30.40	0.86	35.04	1.04	38.89	1.21	41.86	1.21
76	45	1	1	2.67	0.22	3.24	0.24	3.77	0.29	4.23	0.33	5.07	0.31
77	45	1	2	4.20	0.29	5.14	0.32	6.04	0.38	6.76	0.41	8.10	0.39
78	45	1	3	5.59	0.33	6.80	0.37	7.95	0.44	8.78	0.48	10.50	0.46
79	45	1	5	8.17	0.39	9.45	0.47	11.17	0.51	12.32	0.59	13.94	0.57
80	45	1	10	13.46	0.49	15.43	0.66	17.89	0.71	19.98	0.78	21.68	0.78
81	45	2	1	3.68	0.27	4.29	0.32	4.84	0.39	5.57	0.42	6.32	0.43
82	45	2	2	5.34	0.35	6.46	0.41	7.63	0.47	8.60	0.52	10.09	0.52
83	45	2	3	6.99	0.39	8.43	0.46	9.97	0.52	10.92	0.59	13.07	0.59

84	45	2	5	9.73	0.45	11.51	0.45	13.55	0.63	15.00	0.69	17.52	0.70
85	45	2	10	15.53	0.60	18.07	0.60	20.94	0.81	24.02	0.90	26.58	0.94
86	45	3	1	4.58	0.30	5.20	0.38	5.90	0.46	6.58	0.52	7.50	0.52
87	45	3	2	6.41	0.38	7.48	0.47	8.87	0.54	9.88	0.62	11.59	0.63
88	45	3	3	8.19	0.44	9.60	0.52	11.51	0.61	12.67	0.69	14.82	0.70
89	45	3	5	11.25	0.50	13.08	0.62	15.49	0.69	17.28	0.78	20.02	0.81
90	45	3	10	17.64	0.66	20.20	0.79	23.50	0.91	26.69	0.98	30.34	1.04
91	45	5	1	6.30	0.36	6.92	0.43	7.69	0.55	8.45	0.60	9.53	0.64
92	45	5	2	8.35	0.45	9.63	0.54	11.03	0.66	11.99	0.73	13.96	0.77
93	45	5	3	10.26	0.52	11.85	0.62	13.71	0.75	15.26	0.79	17.30	0.85
94	45	5	5	13.47	0.61	15.60	0.72	18.54	0.83	20.90	0.87	23.25	0.94
95	45	5	10	21.04	0.74	24.40	0.88	28.12	1.00	31.39	1.15	33.86	1.26
96	45	10	1	9.20	0.29	9.99	0.33	10.56	0.41	11.78	0.44	12.39	0.51
97	45	10	2	11.43	0.37	12.78	0.44	14.29	0.54	15.55	0.59	17.32	0.68
98	45	10	3	13.58	0.43	15.38	0.53	17.53	0.63	19.13	0.70	21.26	0.79
99	45	10	5	17.11	0.53	20.03	0.63	22.81	0.75	25.26	0.83	27.88	0.92
100	45	10	10	25.42	0.69	29.52	0.85	33.66	1.02	37.53	1.19	40.73	1.23
101	60	1	1	2.48	0.25	3.04	0.32	3.68	0.30	4.08	0.34	4.67	0.36
102	60	1	2	3.91	0.31	4.90	0.37	5.94	0.37	6.40	0.42	7.44	0.44
103	60	1	3	5.18	0.36	6.52	0.41	7.72	0.42	8.39	0.49	9.65	0.51
104	60	1	5	7.50	0.41	9.29	0.50	10.85	0.51	11.46	0.59	13.62	0.63
105	60	1	10	12.20	0.58	15.19	0.63	17.15	0.70	19.07	0.76	21.28	0.86
106	60	2	1	3.45	0.30	4.10	0.34	4.69	0.39	5.13	0.44	5.89	0.49
107	60	2	2	5.07	0.36	6.12	0.43	7.17	0.48	7.83	0.53	9.01	0.58
108	60	2	3	6.43	0.41	7.87	0.50	9.43	0.54	10.30	0.59	11.65	0.66
109	60	2	5	9.09	0.49	11.08	0.49	12.70	0.65	14.06	0.67	16.27	0.79
110	60	2	10	14.50	0.65	17.73	0.65	20.35	0.80	22.49	0.88	24.67	1.04
111	60	3	1	4.34	0.34	4.93	0.40	5.76	0.45	6.19	0.53	6.95	0.57
112	60	3	2	5.94	0.42	7.14	0.49	8.39	0.54	9.41	0.60	10.31	0.68
113	60	3	3	7.48	0.48	9.10	0.55	10.70	0.61	12.16	0.64	13.35	0.76
114	60	3	5	10.31	0.56	12.70	0.63	14.40	0.70	16.44	0.75	17.99	0.92
115	60	3	10	16.20	0.72	19.83	0.81	22.95	0.89	25.42	1.00	27.26	1.23
116	60	5	1	5.98	0.37	6.59	0.45	7.42	0.54	8.00	0.62	8.75	0.66
117	60	5	2	7.73	0.46	9.19	0.56	10.28	0.65	11.77	0.72	12.72	0.77
118	60	5	3	9.48	0.53	11.46	0.63	13.06	0.71	14.81	0.78	16.19	0.86
119	60	5	5	12.74	0.62	15.14	0.74	17.98	0.81	19.28	0.91	21.40	1.02
120	60	5	10	19.43	0.78	23.51	0.96	26.93	1.00	29.63	1.16	32.63	1.34
121	60	10	1	8.93	0.28	9.46	0.32	10.43	0.38	10.79	0.44	11.72	0.49
122	60	10	2	10.75	0.36	11.93	0.44	13.72	0.51	14.84	0.60	16.51	0.64
123	60	10	3	12.62	0.43	14.41	0.52	16.67	0.62	18.17	0.69	20.06	0.78
124	60	10	5	16.12	0.54	19.27	0.65	21.58	0.76	23.32	0.83	26.32	0.93
125	60	10	10	23.89	0.70	28.12	0.88	32.03	0.98	35.41	1.13	38.20	1.27
126	75	1	1	2.46	0.24	2.85	0.27	3.20	0.31	3.67	0.35	3.93	0.37
127	75	1	2	3.74	0.31	4.51	0.34	5.21	0.39	5.78	0.42	6.24	0.46

128	75	1	3	4.98	0.36	6.02	0.39	6.98	0.45	7.56	0.50	8.27	0.53
129	75	1	5	7.18	0.42	8.41	0.47	9.89	0.54	10.52	0.62	11.11	0.66
130	75	1	10	11.75	0.60	13.84	0.65	15.81	0.73	17.76	0.85	18.13	0.89
131	75	2	1	3.38	0.33	3.88	0.37	4.28	0.43	4.84	0.47	5.23	0.49
132	75	2	2	4.77	0.42	5.64	0.46	6.35	0.52	7.35	0.58	7.73	0.61
133	75	2	3	6.14	0.46	7.36	0.51	8.32	0.57	9.39	0.67	9.77	0.68
134	75	2	5	8.67	0.55	10.06	0.55	11.71	0.68	12.63	0.79	13.33	0.80
135	75	2	10	13.80	0.72	16.19	0.72	18.35	1.00	20.14	1.10	21.05	1.09
136	75	3	1	4.22	0.37	4.67	0.45	5.16	0.51	5.75	0.58	6.14	0.60
137	75	3	2	5.68	0.46	6.63	0.54	7.41	0.59	8.42	0.67	8.88	0.71
138	75	3	3	6.98	0.54	8.35	0.59	9.51	0.65	10.52	0.78	11.12	0.79
139	75	3	5	9.65	0.62	11.50	0.67	13.16	0.76	14.12	0.91	14.73	0.92
140	75	3	10	15.09	0.83	18.13	0.96	20.71	1.02	22.55	1.28	23.43	1.21
141	75	5	1	5.72	0.43	6.32	0.53	6.69	0.61	7.48	0.70	8.04	0.73
142	75	5	2	7.45	0.54	8.58	0.62	9.48	0.72	10.23	0.87	10.71	0.89
143	75	5	3	9.00	0.62	10.55	0.70	11.58	0.81	12.89	0.98	13.28	0.97
144	75	5	5	11.82	0.74	13.82	0.80	15.91	0.92	17.18	1.14	17.86	1.08
145	75	5	10	18.15	1.00	21.20	1.10	23.85	1.25	26.33	1.52	27.88	1.37
146	75	10	1	8.92	0.28	9.27	0.32	9.94	0.38	10.45	0.44	11.02	0.48
147	75	10	2	10.64	0.39	11.33	0.48	12.70	0.56	13.85	0.65	14.25	0.70
148	75	10	3	12.54	0.48	13.78	0.58	15.05	0.70	16.63	0.81	17.13	0.85
149	75	10	5	15.50	0.63	17.37	0.75	19.58	0.87	20.96	1.05	22.38	1.01
150	75	10	10	22.59	0.88	25.47	1.07	28.75	1.26	31.12	1.58	34.34	1.45

Table 5 The cohesion and inter-frictional angle of specimens under different simulation conditions

No.	α (°)	v (1e-6m/s)	S_h=30%		S_h=40%		S_h=50%		S_h=60%		S_h=70%	
			c (MPa)	ϕ (°)	c (MPa)	ϕ (°)	c (MPa)	ϕ (°)	c (MPa)	ϕ (°)	c (MPa)	ϕ (°)
1	0	1	0.8	15.11	0.95	17.74	0.98	19.8	1.1	20.81	1.25	21.55
2	0	2	1.18	19.29	1.48	20.81	1.8	21.8	2.05	22.78	2.2	24.23
3	0	3	1.83	17.56	2.2	19.42	2.53	20.88	2.85	22.46	3.14	23.33
4	0	5	2.6	19.56	3.02	21.79	3.4	23.8	3.76	25.43	4.2	26.53
5	0	10	4.14	23.25	4.55	26.67	5.1	28.14	5.32	30.56	6.1	30.9
6	15	1	0.82	16.7	0.95	17.75	1.2	17.7	1.45	18.26	1.56	19.8
7	15	2	1.1	20.81	1.35	21.8	1.6	22.78	2.02	22.78	2.3	24.23
8	15	3	1.87	18.4	2.23	19.35	2.53	20.8	2.87	21.71	3.25	22.81
9	15	5	2.69	20.03	3.01	22.27	3.46	23.8	3.61	25.6	4.04	25.92
10	15	10	4.1	24.18	4.6	26.33	5.34	27.69	5.45	30.24	5.79	31.3
11	30	1	0.85	16.44	1.02	16.96	1.05	19.29	1.4	18.78	1.4	20.46
12	30	2	1.25	19.29	1.62	19.33	1.7	22.78	2.05	23.03	2.2	24.23
13	30	3	1.87	17.65	2.25	19.16	2.6	20.91	2.9	21.77	3.29	22.91
14	30	5	2.64	19.99	3.15	21.57	3.54	23.65	3.58	25.88	4.22	26.56
15	30	10	4.17	23.9	4.72	24.39	5.26	28.6	5.56	30.47	5.77	31.69
16	45	1	0.8	17.25	0.92	18.26	1.08	18.78	1.35	18.78	1.45	20.81
17	45	2	1.13	19.94	1.42	20.91	1.68	22.41	1.91	23.04	2.22	24.81
18	45	3	1.92	17.65	2.34	18.52	2.75	19.83	2.97	21	3.61	21.36
19	45	5	2.8	19.1	3.13	21.29	3.66	22.78	3.93	24.48	4.51	25.28
20	45	10	4.29	23.43	4.7	25.91	5.3	27.7	5.85	29.18	6.35	30.24
21	60	1	0.62	17.75	0.93	17.22	1.1	18.26	1.25	18.26	1.5	18.78
22	60	2	1.34	15.77	1.74	16.15	2.03	17.36	2.21	18.48	2.49	19.35
23	60	3	1.79	16.81	2.27	17.63	2.65	19.07	2.88	20.37	3.22	21.24
24	60	5	2.58	18.67	3.098	20.57	3.53	21.99	3.81	22.99	4.33	24.04
25	60	10	3.94	22.9	4.8	24.29	5.27	26.59	5.67	28.1	6.17	28.94
26	75	1	0.65	16.7	0.82	17.22	0.95	17.22	1.18	17.48	1.18	19.29
27	75	2	1.23	15.96	1.58	15.82	1.76	16.98	2.01	17.58	2.18	17.55
28	75	3	1.64	17.07	2.07	17.36	2.4	17.81	2.59	19.19	2.8	18.99
29	75	5	2.45	18.15	2.9	19.12	3.35	20.24	3.52	21.27	3.6	22.32
30	75	10	3.83	21.8	4.54	22.78	5.03	24.37	5.53	25.11	5.25	28.07

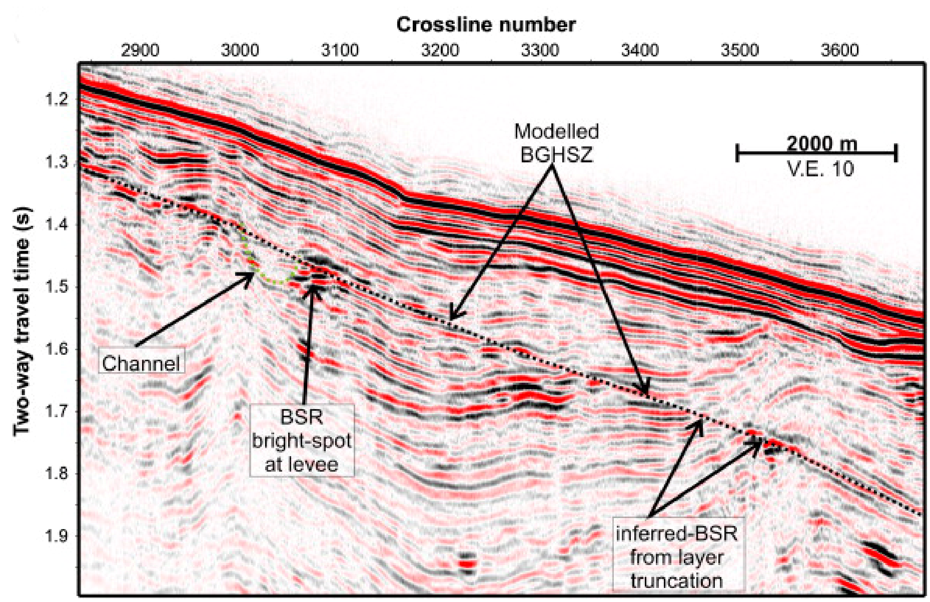

Fig. 1 A seismic section from the 3D PSTM volume with stratigraphic interpretation at Krishna-Godavari Basin showing the BSR and hydrate mound (Riedel et al., 2011).

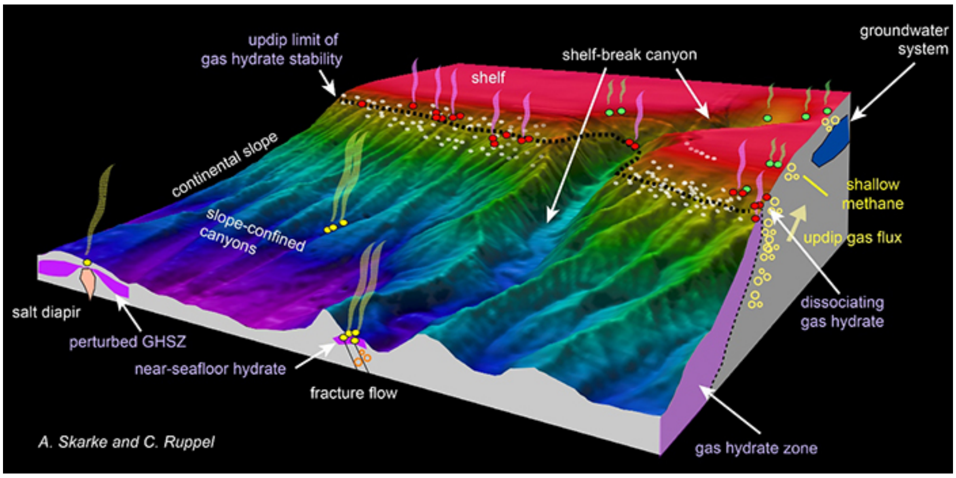

Fig. 2 Schematic showing the general setting of seeps on the US Atlantic margin and related processes (Skarke et al., 2014)

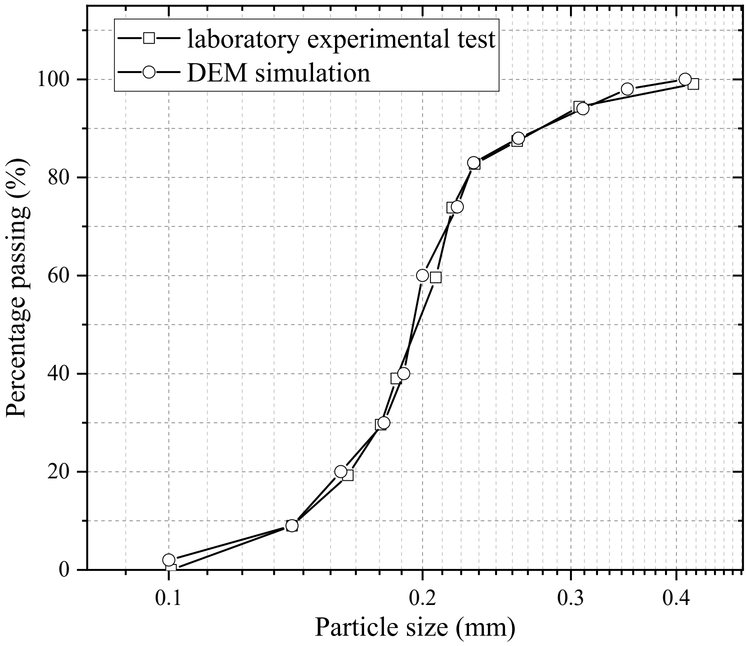

Fig. 3 The particle size distribution of soil grains in simulation and experimental test.

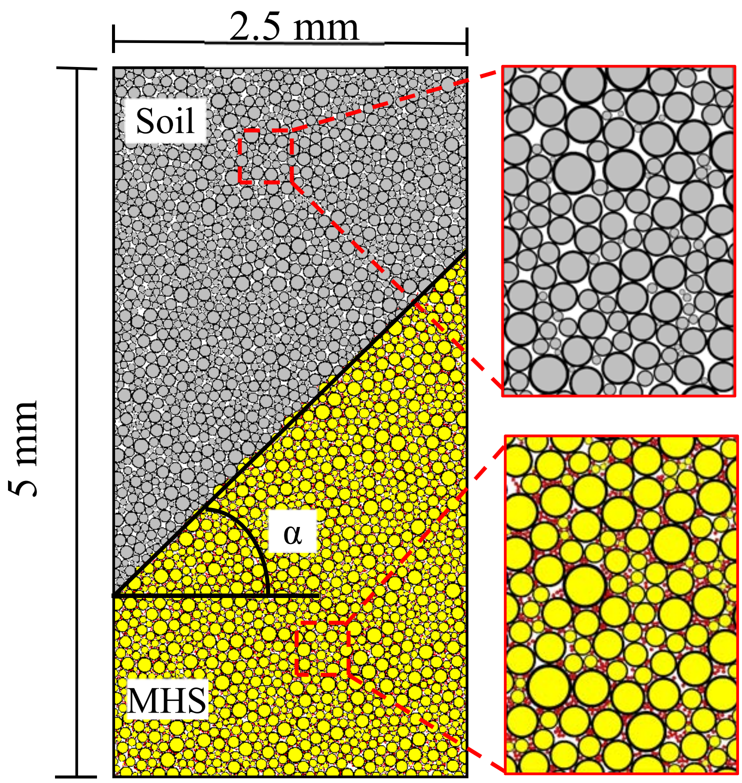

Fig. 4 DEM simulation model of methane hydrate considering deposit angle

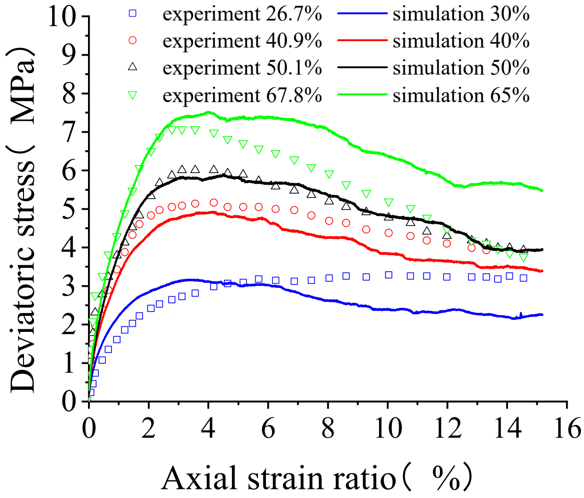

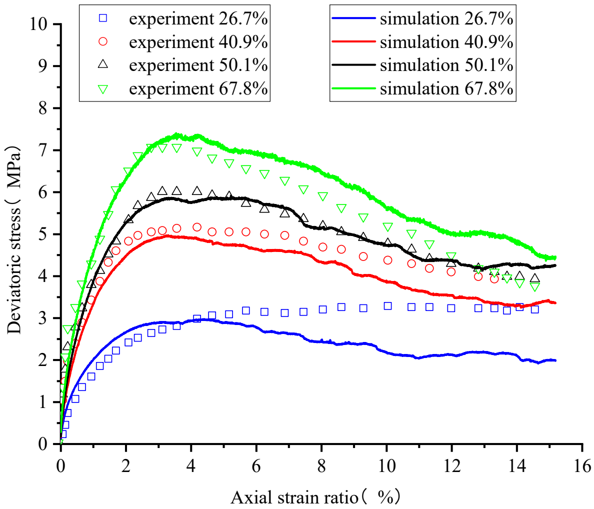

Fig. 5 Deviatoric stress versus axial strain ratio in simulating tests and experimental tests

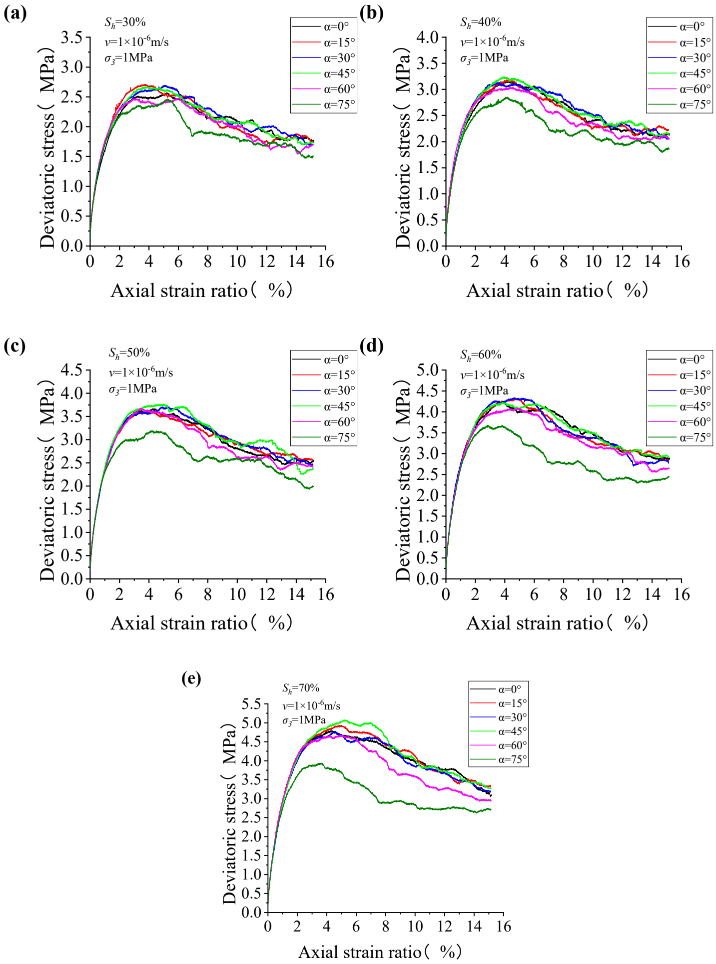

Fig. 6 Deviatoric stress versus axial strain ratio under different deposit angle conditions

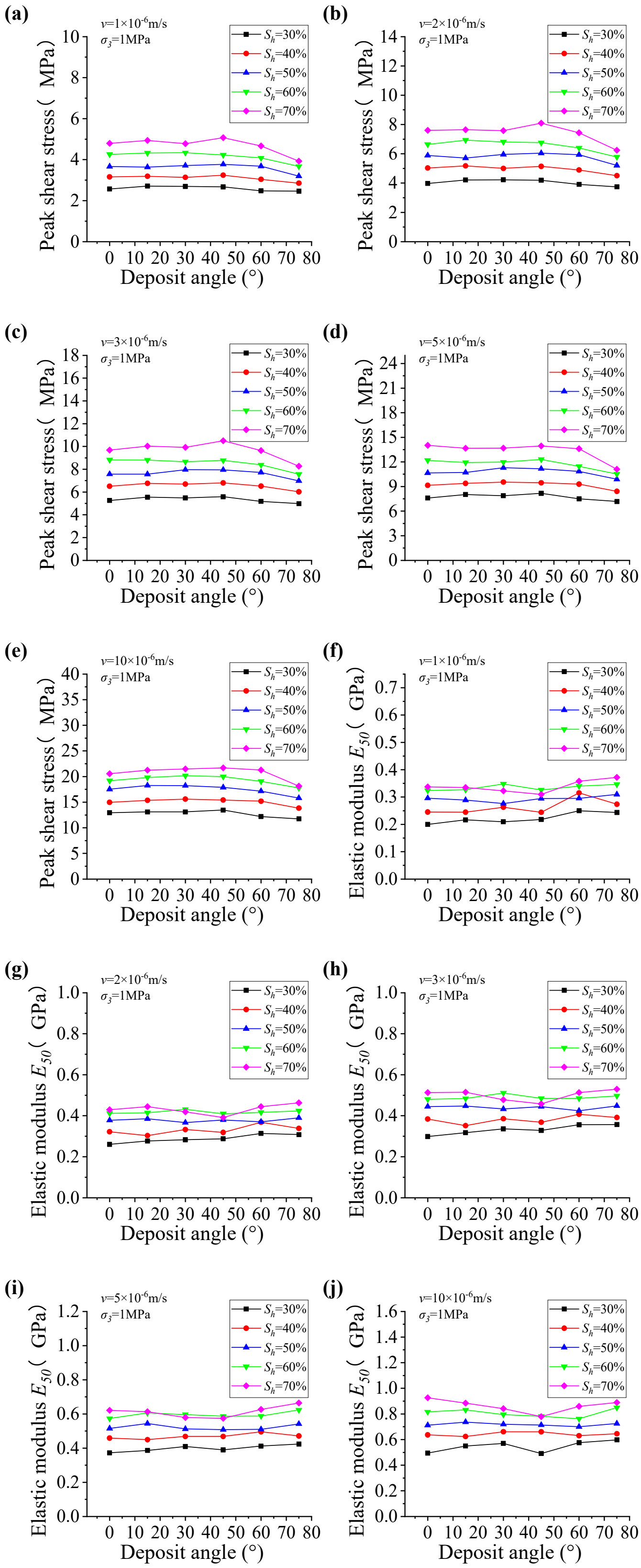

Fig. 7 Peak stress (a)~(e) and elastic modulus (f)~(j) versus deposit angle under different loading velocities and S_h conditions

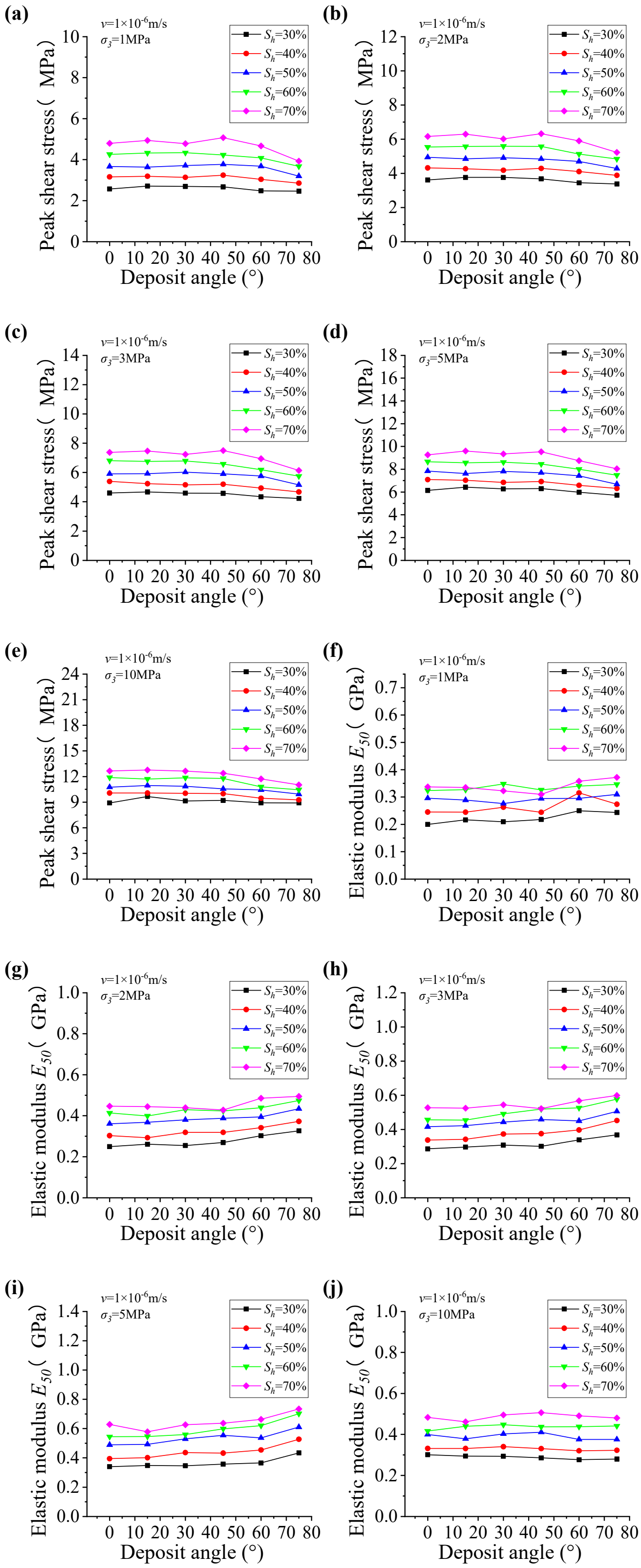

Fig. 8 Peak stress (a)~(e) and elastic modulus (f)~(j) versus deposit angle under different confining pressure and S_h conditions

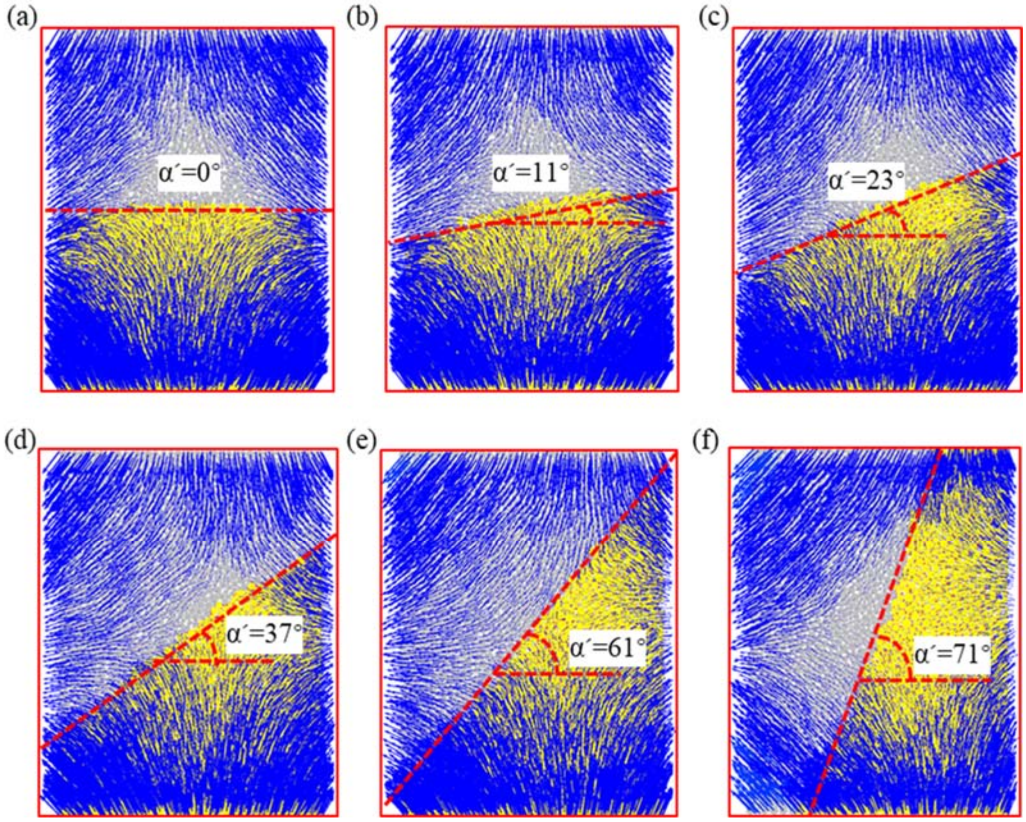

Fig. 9 Displacement (blue line with arrows) and final deposit angle (α′) distribution of samples after shear test under the condition that the confining pressure was 1 MPa, the hydrate saturation was 70% and the loading velocity was 1×10^{-6}m/s. The initial deposit angle were (a) α=0°, (b) α=15°, (c) α=30°, (d) α=45°, (e) α=60°, (f) α=75°

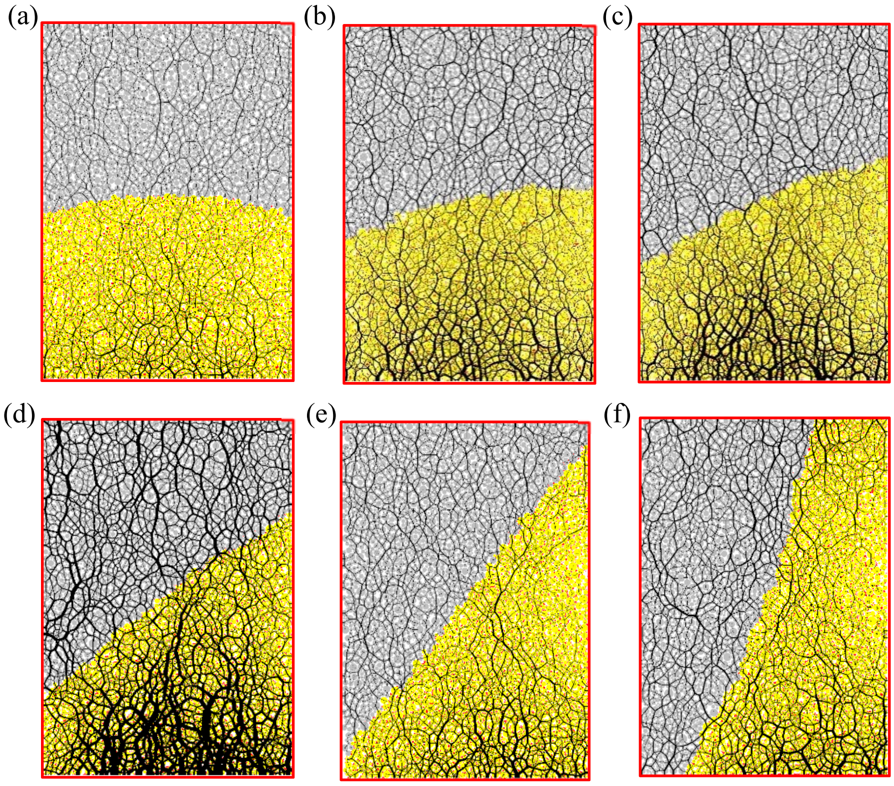

Fig. 10 The contact force distribution of samples after shear test under the condition that the confining pressure was 1 MPa, the hydrate saturation was 70% and the loading velocity was 1×10^{-6}m/s. The initial deposit angle were (a) α=0°, (b) α=15°, (c) α=30°, (d) α=45°, (e) α=60°, (f) α=75°

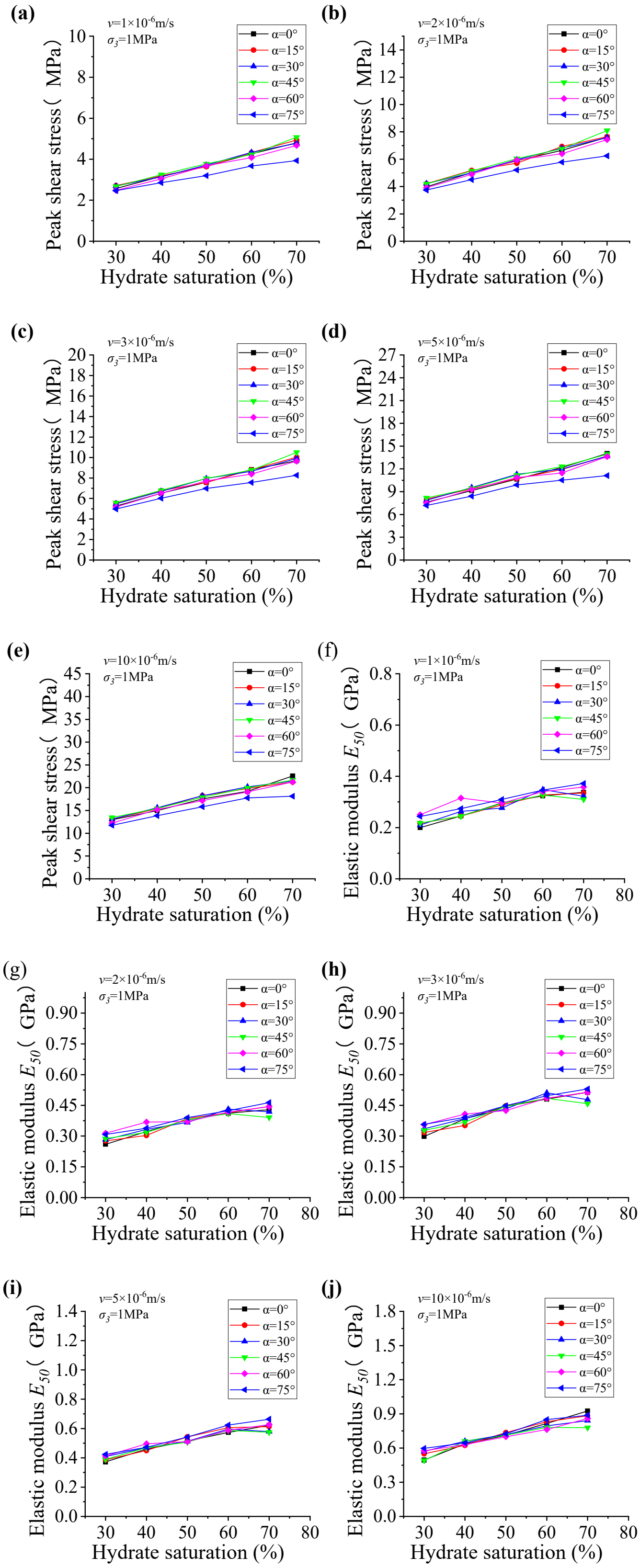

Fig. 11 Peak stress (a)~(e) and elastic modulus (f)~(j) versus hydrate saturation under different loading velocities and deposit angle conditions

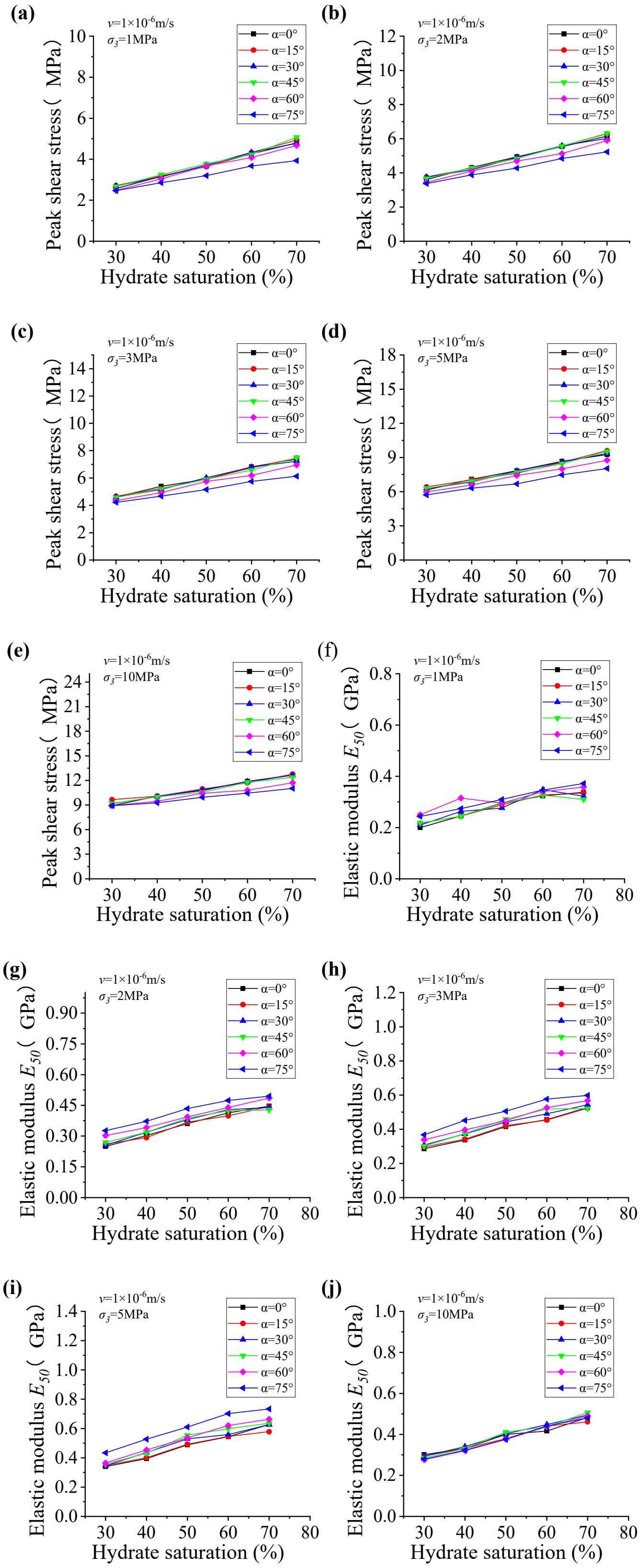

Fig. 12 Peak stress (a)~(e) and elastic modulus (f)~(j) versus hydrate saturation under different confining pressure and deposit angle conditions

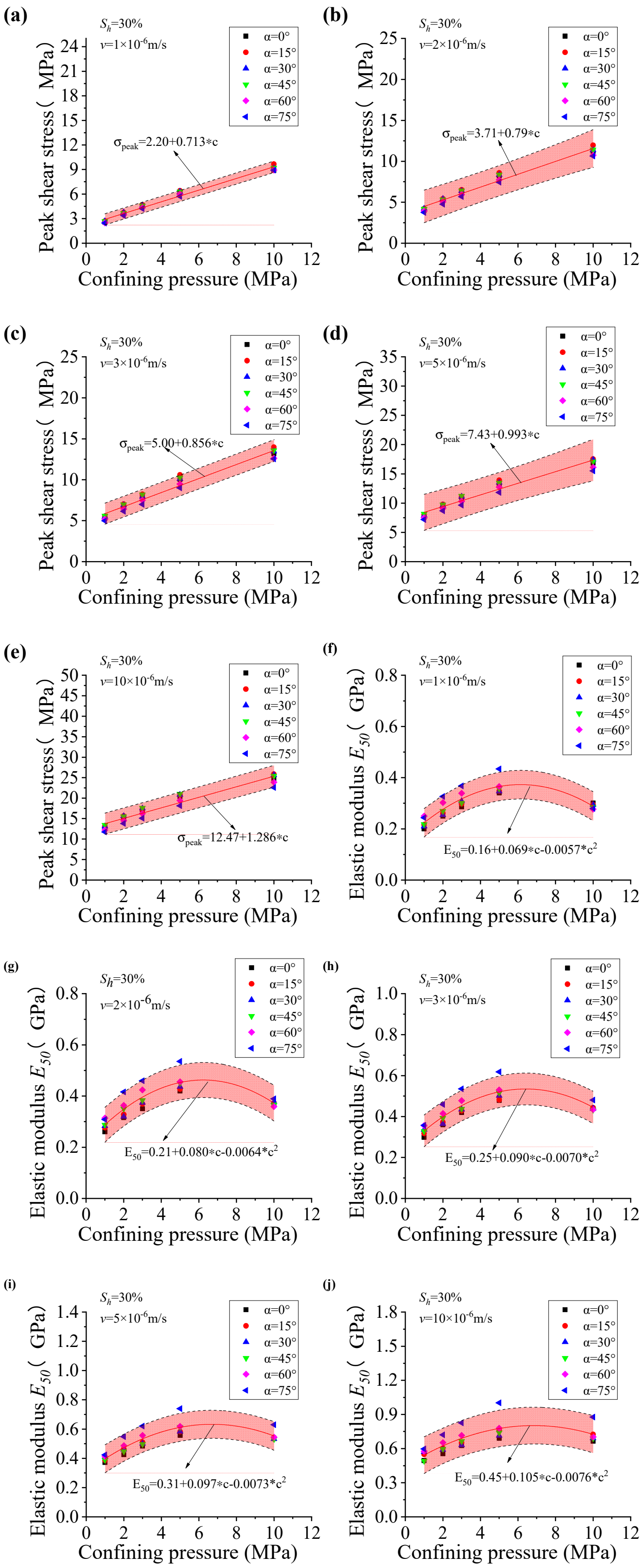

Fig. 13 Peak stress (a)~(e) and elastic modulus (f)~(j) versus confining pressure under different loading velocities and deposit angle conditions

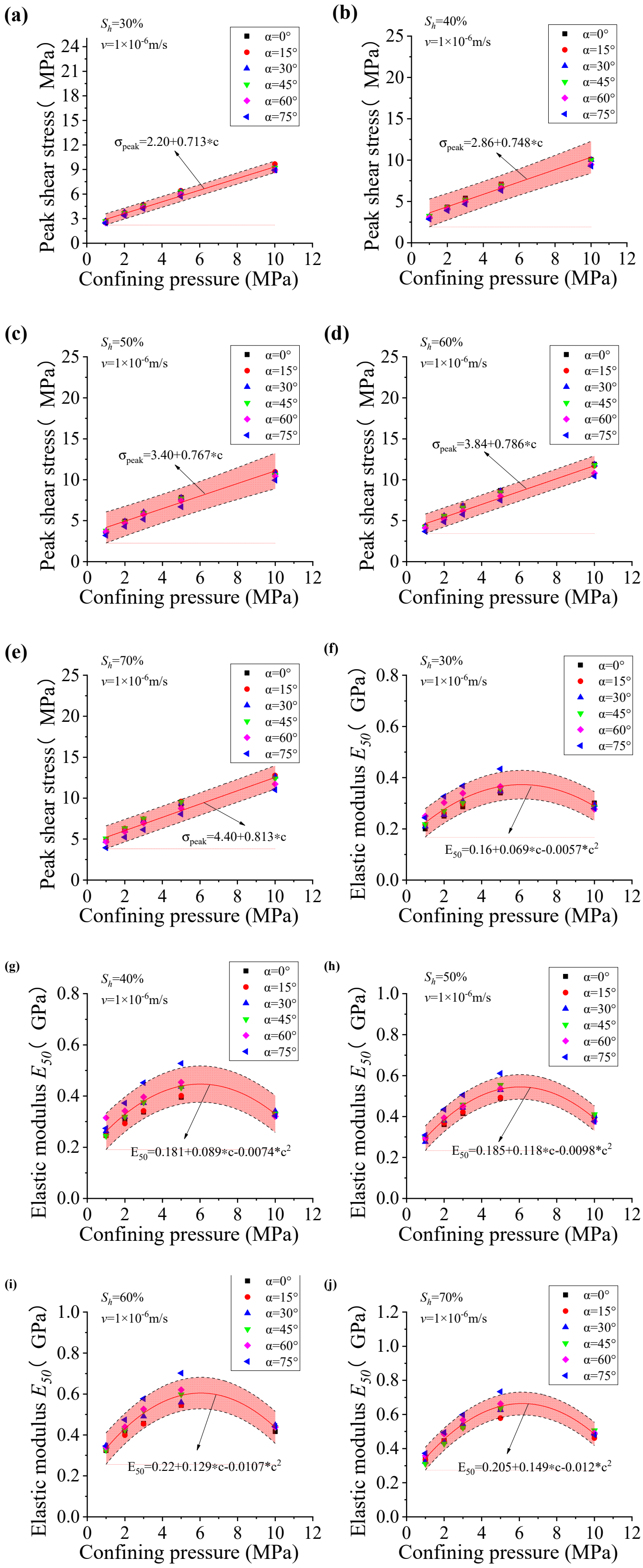

Fig. 14 Peak stress (a)~(e) and elastic modulus (f)~(j) versus confining pressure under different hydrate saturation and deposit angle conditions

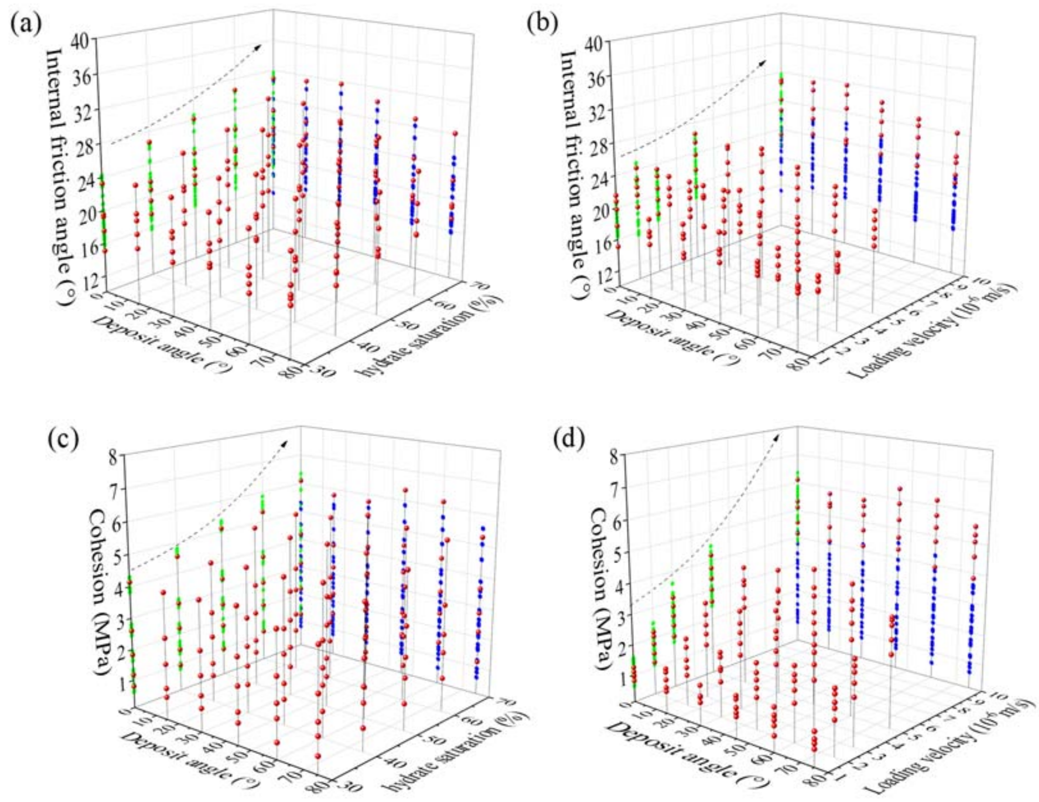

Fig. 15 Relationships between internal friction angle (a) versus deposit angle and hydrate saturation (b) versus deposit angle and loading velocity and relationships between cohesion (c) versus deposit angle and hydrate saturation (d) versus deposit angle and loading velocity. The red balls represent the initial data and the blue points and the green points represent the projection points.

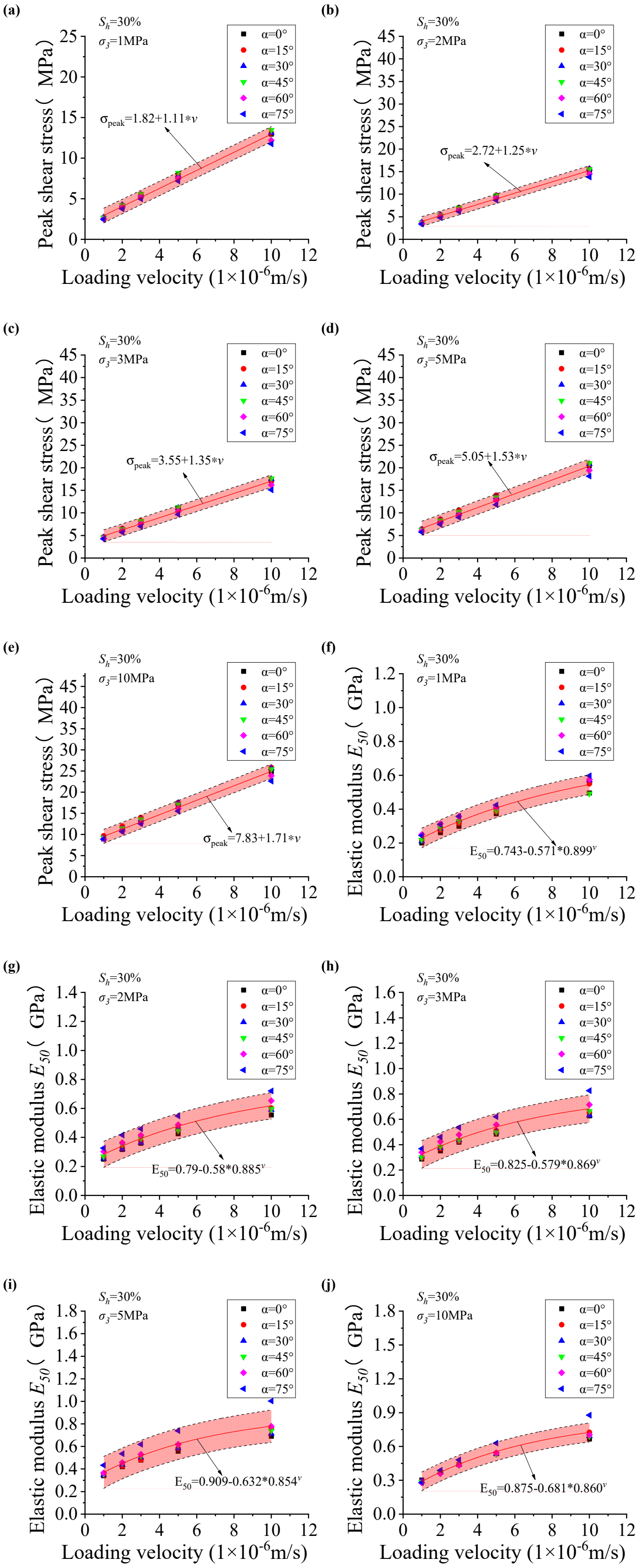

Fig. 16 Peak stress (a)~(e) and elastic modulus (f)~(j) versus loading velocity under different confining pressure and deposit angle conditions

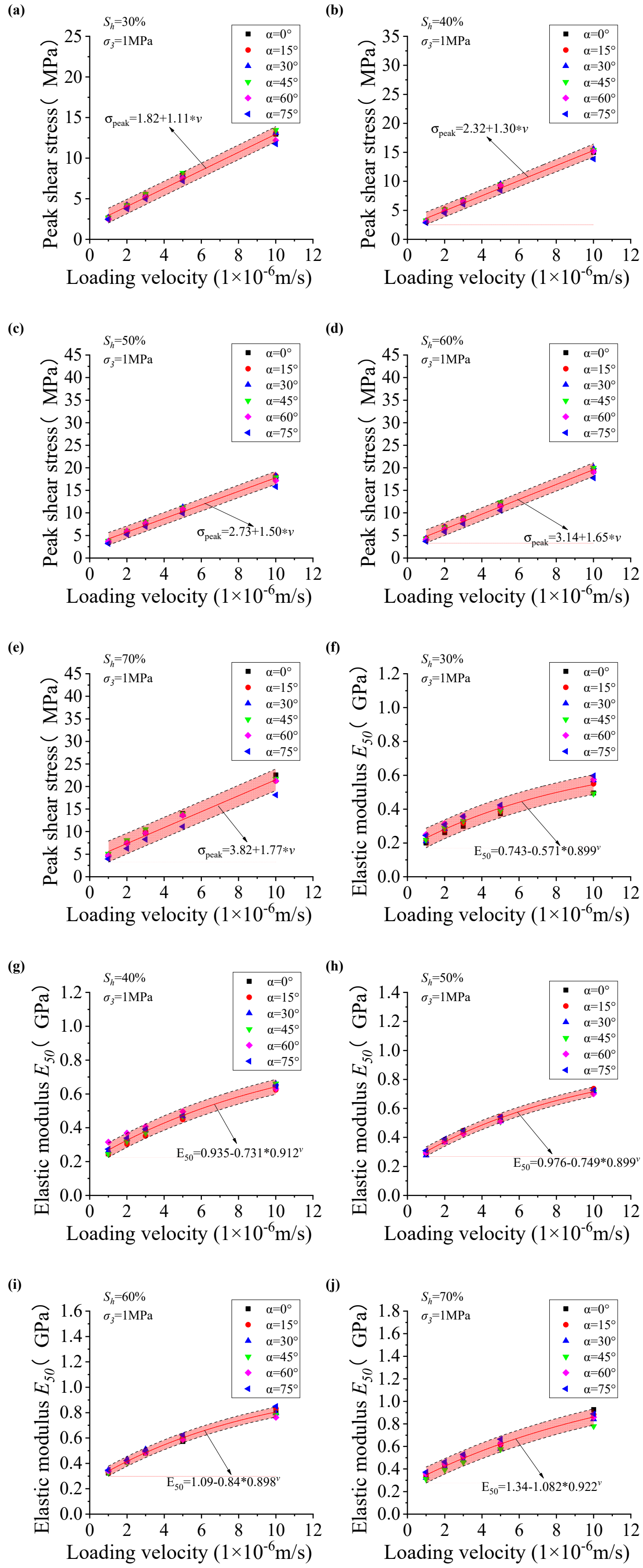

Fig. 17 Peak stress (a)~(e) and elastic modulus (f)~(j) versus loading velocity under different hydrate saturation and deposit angle conditions